Arabian Journal of Chemistry (2020) **13**, 2806–2825

King Saud University

Arabian Journal of Chemistry

www.ksu.edu.sa
www.sciencedirect.com

ORIGINAL ARTICLE

Hydrothermal synthesis, structural characterization and photocatalytic properties of β-Ag_2MoO_4 microcrystals: Correlation between experimental and theoretical data

Giancarlo da Silva Sousa [a,g], Francisco Xavier Nobre [b,c], Edgar Alves Araújo Júnior [a], Julio Ricardo Sambrano [d], Anderson dos Reis Albuquerque [e], Rosane dos Santos Bindá [c], Paulo Rogério da Costa Couceiro [c], Walter Ricardo Brito [c], Laécio Santos Cavalcante [f], Maria Rita de Morais Chaves Santos [a,*], José Milton Elias de Matos [a,*]

[a] *Laboratório Interdisciplinar de Materiais Avançados, LIMAV-UFPI, Universidade Federal do Piauí, CEP 69049-550, Teresina, PI, Brazil*
[b] *Instituto Federal de Educação, Ciência e Tecnologia do Amazonas, Campus Coari, IFAM-CCO-AM, CEP 69460-000, AM, Brazil*
[c] *Laboratório de Físico-Química, LFQ-UFAM, Universidade Federal do Amazonas, CEP 69077-000, Manaus, AM, Brazil*
[d] *Grupo de Modelagem e Simulação Molecular, INCTMN-UNESP, São Paulo State University, CEP 17033-360, Bauru, SP, Brazil*
[e] *Instituto de Química, Universidade Federal do Rio Grande do Norte (UFRN), Natal-RN, CEP 59078-970, Brazil*
[f] *PPGQ-CCN-GERATEC, Universidade Estadual do Piauí, Rua: João Cabral, N. 2231, P.O. Box 381, 64002-150 Teresina, PI, Brazil*
[g] *Centro Universitário Santo Agostinho – UNIFSA, Av. Valter alencar 665 – Bairro São Pedro, CEP 64019-625, Teresina, PI, Brazil*

Received 31 January 2018; accepted 11 July 2018
Available online 20 July 2018

KEYWORDS

β-Ag_2MoO_4 microcrystals;
Theoretical calculations;
Band gap;
Coral-like;
Photocatalytic properties

Abstract In this paper, we report about hydrothermal synthesis, structural characterization and photocatalytic properties of beta-silver molybdate (β-Ag_2MoO_4) microcrystals obtained at different temperatures (100, 120, 140 and 160 °C) for 2 h. These crystals were characterized structurally using X-ray diffraction (XRD), X-ray fluorescence, Rietveld refinement, micro-Raman (m-Raman) and Fourier-transform infrared (FT-IR) spectroscopies. Experimental and theoretical band gap values were correlated by ultraviolet–visible (UV–Vis) diffuse reflectance spectroscopy and periodic

* Corresponding authors.
E-mail addresses: francisco.nobre@ifam.edu.br (F.X. Nobre), mrita@ufpi.edu.br (M.R.d.M.C. Santos), jmematos@ufpi.edu.br (J.M.E. de Matos).

Peer review under responsibility of King Saud University.

Production and hosting by Elsevier

https://doi.org/10.1016/j.arabjc.2018.07.011

first-principles calculations in the framework of density functional theory (DFT) with the B3LYP-D3 hybrid functional. The crystals morphology was observed through field-emission scanning electron microscopy (FE-SEM) images. The photocatalytic properties of these crystals were investigated for degradation of rhodamine B (RhB) dye under UV-light. XRD patterns and Rietveld refinement data indicate that all crystals exhibit a spinel-type cubic structure with space group ($Fd3'm$) formed by tetrahedral [MoO_4] clusters and distorted octahedral [AgO_6] clusters. m-Raman spectra exhibited five Raman-active modes in a range from 50 to 1000 cm^{-1}, while FT-IR spectra have three infrared active modes in a range from 400 to 1100 cm^{-1}. The experimental results from Raman and IR modes are in reasonable agreement with theoretically calculated results. Experimental UV–Vis spectra indicate a decrease in optical band gap (E_{gap} = 3.35 eV to 3.32 eV) with the temperature rise. The calculated band structure revealed an indirect optical band gap (E_{gap}) of approximately 3.94 eV. Moreover, theoretical calculations based on density of states and electron density maps were employed to understand the polarization phenomenon induced by structural defects in the β-Ag_2MoO_4 microcrystals. FE-SEM images revealed that the increase of processing temperatures promotes a change in shape of microcrystals from potatoes-like to coral-like. Finally, photocatalytic measures to degradation of the RhB dye resulted in the best catalytic performance for β-Ag_2MoO_4 microcrystals synthesized at temperatures of 120 and 140 °C, corresponding to 97.3% and 96.8% in the photodegradation of RhB dye under UV–light up to 2 h. The stability of the β-Ag_2MoO_4 was investigated by reusing, resulting in f 97.2, 93.9 and 78.8% degradation of the RhB dye for the first, second and third cycle, respectively.

1. Introduction

Silver molybdates (Ag_2MoO_4) crystals are known as indirect semiconductors, which have aroused great interest from the scientific community and electronic industry due to their optical properties satisfactory (Cunha et al., 2015; Gupta et al., 2015), antifungal (Fabbro et al., 2016), electrical (Feng et al., 2011), photocatalytic degradation of chronic toxicity ciprofloxacin and highly selective electrochemical detection of H_2O_2 (Kumar et al., 2016), and antimicrobial (Oliveira et al., 2017). According to the literature (Arora et al., 2012; Ng & Fan, 2015; Beltrán et al., 2014), the Ag_2MoO_4 crystals may exhibit two polymorphs: the beta (β) phase is more stable and has a spinel-type cubic structure with space group ($Fd3'm$), and the alpha (α) phase is metastable and has a tetragonal structure with space group ($P4_122$).

The α-Ag_2MoO_4 crystals are irreversible transforms to β-Ag_2MoO_4 crystals upon heating above 280 °C (Arora et al., 2012). Recently, (Moura et al., 2017) have obtained β-Ag_2MoO_4 microcrystals by the hydrothermal method at 160 °C for 1 h and studied by means of micro-Raman spectroscopy with high-temperature measurements. This paper explains that these β-Ag_2MoO_4 microcrystals undergoes a first phase transition from cubic structure to an unknown structure during the heating cycle above around 268 °C, and occurs a second phase transition occurs at around 427 °C related to crystal changes its unknown structure to a cubic structure. However, a theoretical work (Beltrán et al., 2014) have explained that the Ag_2MoO_4 crystals exhibit four phase transitions under pressure. The first phase has a tetragonal structure (with normal and inverse space group $P4_122$) above 15 GPa, and the second phase has a cubic structure (ascribed to β-Spinel-type) at ambient pressure, the third phase an orthorhombic structure (ascribed as Olivine-type) and the fourth phase has a tetragonal structure (ascribed to α-K_2NiF_4-type) at above 6 GPa. In addition, the literature (Singh et al., 2012) have investigated the pH effect on the formation of the self-assembly of monoclinic $Ag_2(Mo_2O_7)$ micro-rods at pH = 3 and 4, with the flower-like morphology of mixed phase of monoclinic and triclinic $Ag_2Mo_2O_7$ at (pH = 5) and the formation of β-Ag_2MoO_4 microparticles at (pH = 7 and 8).

In relation to synthesis methods to obtain α-Ag_2MoO_4 or β-Ag_2MoO_4 microcrystals, have been observed a significant advance and evolution for optimization of these crystals with controlled size and shape (Wang et al., 2017; Ng and Fan, 2017, Zhang and Ma, 2017a,b, Tang et al., 2017) to photocatalytic activity for degradation of different organic dyes (Rhodamine B, methyl orange, and methylene blue). However, these papers reported have not shown a correlation between their experimental data with quantum mechanical calculations.

Therefore, in this paper, we report on the synthesis of β-Ag_2MoO_4 microcrystals by the conventional hydrothermal without surfactants at different temperatures (100, 120, 140 e 160 °C) for 2 h. These microcrystals obtained were characterized structurally by means of X-ray diffraction (XRD), X-ray fluorescence, Rietveld refinement, micro-Raman (m-Raman) and Fourier-transform infrared (FT-IR) spectroscopies. Morphological aspects were investigated by Field-emission scanning electron microscopy (FE-SEM) images. The optical band gaps of microcrystals were found by ultraviolet–visible (UV–vis) diffuse reflectance spectroscopy. The electronic band structure, density of states (DOS) and electron density maps of β-Ag_2MoO_4 were theoretically calculated to understand the phenomenon of structural order-disorder to the improvement of the photocatalytic (PC) properties for degradation of Rhodamine B (RhB) dye under UV-light.

2. Experimental details

2.1. Synthesis of β-Ag_2MoO_4 microcrystals by the CH method

The synthesis of β-Ag_2MoO_4 microcrystals is described as follows: 1×10^{-3} mols of molybdate sodium dihydrate

($Na_2MoO_4{\cdot}2H_2O$; 99.5% purity, Sigma-Aldrich) and 2×10^{-3} mols of silver nitrate ($AgNO_3$; 99.8% purity, Sigma-Aldrich) were separately dissolved 45 mL of deionized water for each salt, in two plastic tubes (Falcon - capacity of 50 mL). These two solutions were then transferred into a Teflon autoclave (capacity of 150 mL) in a conventional hydrothermal (CH) system, which remained under magnetic stirring for 10 min, finally obtaining a light beige suspension. CH reactions were performed at different temperatures (100, 120, 140, and 160 °C) for 2 h. In principle, β-Ag_2MoO_4 microcrystals were obtained by the reaction between $2Ag^+ \leftarrow: MoO_4^{2-}$ ions as described in Eqs. (1)–(3):

$$Na_2MoO_4 \cdot 2H_2O_{(s)} \xrightarrow{H_2O(25\,^\circ C)} 2Na^+_{(aq)} + MoO^{2-}_{4(aq)} + 2H_2O \quad (1)$$

$$2AgNO_{3(s)} \xrightarrow{H_2O(25\,^\circ C)} 2Ag^+_{(aq)} + 2NO^-_{3(aq)} \quad (2)$$

$$2Ag^+(aq) + 2NO_3^-(aq) + 2Na^+(aq) + MoO_4^{-2}(aq) + 2H_2O(l) \xrightarrow{HC(\Delta T\ =\ 100to160\ ^\circ C;t\ =\ 2h)} \beta - Ag_2MoO_4(s) + 2NO^{-3}(aq) + 2Na^+(aq) + 2H_2O(l) \quad (3)$$

The obtained light beige suspension was washed with deionized water several times to remove any remaining Na^+ and NO_3^- ions. These crystals were separated by means of centrifugations at 4000 rpm for 10 min for seven times. Finally, these powders were oven dried at 75 °C for 12 h, then stored for further characterization and catalytic testing.

2.2. Characterization of β-Ag_2MoO_4 microcrystals

β-Ag_2MoO_4 microcrystals were structurally characterized by XRD patterns using a LabX XRD-6000 diffractometer (Shimadzu®, Japan) with Cu-Kα radiation (λ = 0.15406 nm) in the 2θ range from 10° to 80° with a scanning velocity of 2°/min. Rietveld analysis was conducted in the same range with a scanning velocity of 1°/min and a step of 0.02°. The semi-quantitative analyzes were obtained by X-ray fluorescence (XRF) using PANalytical, Epsilon 3^x (Netherlands) equipment, with Rhodium (Rh) silver (Ag) and molybdenum (Mo) excitation tubes operating under Voltage of 40 KV and current of 3 mA. The methodology adopted includes the "loose powder", accommodating about 1.5 g of the microcrystals in polyethylene sample holders with dimensions of 2.5 cm (diameter) by 4 cm (height), sealed with films of propylene. M-Raman spectra were recorded using a SENTERRA spectrometer (Bruker®, Germany) equipped with He–Ne laser (λ = 532 nm) and CCD operating from 50 cm^{-1} to 950 cm^{-1}. The incident laser beam power on the sample was kept at 0.2 mW. For the region located between 85 cm^{-1} and 1000 cm^{-1}, 100 scans were completed with a spectral resolution of 4 cm^{-1}. A 50 μm lens was used to prevent overheating of the sample. Fourier Transform infrared (FT-IR) spectra were performed from 400 cm^{-1} to 1100 cm^{-1} with a spectrophotometer (Varian®, USA) operated in transmittance mode (model IR 660). UV–vis spectra were taken using a UV-2600 spectrophotometer (Shimadzu®, Japan) in diffuse-reflectance mode, using Barium sulfate ($BaSO_4$, 99.999%, Shimadzu) as analytical standard. Morphological aspects of the microcrystals were verified with FE-SEM using a Quanta SEM 250 microscope (FEI®Company, Netherlands) operated at 15 kV.

2.3. Photocatalytic activity measurement of β-Ag_2MoO_4 microcrystals

The PC properties of β-Ag_2MoO_4 microcrystals for the degradation of RhB [$C_{28}H_{31}ClN_2O_3$] (99.5% purity, Mallinckrodt, dissolved in water were tested under ultraviolet (UV) light illumination. In this case, 50 mg of catalyst crystals were placed in two beakers (maximum capacity of 250 mL) and then 50 mL of RhB solution (1×10^5 mol L^{-1}) with pH = 4 were added. Before UV illumination, these suspensions were stirred by sonication during 10 min with an ultrasound bath model 1510 (Branson, USA) (frequency of 42 kHz) and stored in the dark for 5 min in order to allow the absorption of RhB dye on the catalysts. In the sequence, the beakers were placed inside a photo-reactor at 25 °C (Lianyungang Hongkang Quartz products Co., Ltd, China) and illuminated by six UV lamps (TUV Osram, 15 W, maximum intensity at λ = 254 nm). At ten-twenty-minute intervals, 3 mL aliquots of these solutions were removed of the PC system, placed in plastic tubes (Falcon) and centrifuged at 4000 rpm for 5 min to separate the crystals from the liquid phase. Finally, variations of the absorption band maximum at λ = 554 nm of RhB dyes were monitored by UV–Vis absorbance measurements using a double-beam spectrophotometer with a double monochromator and a photomultiplier tube detector of Thermo Scientific Instruments (Model Genesys 10S, USA). The stability of the β-Ag_2MoO_4 was investigated by reusing the microcrystals over three consecutive catalytic cycles initially using 50 mL of 5 mg L^{-1} RhB dye solutions together with 50 mg of the catalyst.

2.4. Computational method for β-Ag_2MoO_4 microcrystals

Silver molybdate (β-Ag_2MoO_4) was modeled in bulk phase taking into account the internal and translational symmetry in order to well represent periodic 3D conditions. This allows evaluating ubiquitous long-range properties in the solid, more realistic and consistent with the obtained micrometric material. This β-Ag_2MoO_4 have cubic structure, with space group ($Fd3'm$), defined by one lattice parameter (a = 9.26 Å; V = 794.0 $Å^3$) and three non-equivalent atoms (1 Ag, 1 Mo, and 1O). This structure can be described by molybdenum tetrahedron [MoO_4] clusters linked to silver octahedron [AgO_6] clusters by the vertex. The shared oxygens are also on tetrahedron coordination $O_{(4c)}$ bonded to three Ag and one Mo, forming the [OAg_3Mo] polyhedron (Andrés et al., 2015; Piasecki et al., 2015). The graphical manipulations were performed using the molecular graphics programs XCRYSDEN and VESTA version 3.4.0 for Linux (Kokalj 2003, Momma and Izumi, 2011; Gouveia et al., 2014; Kassou et al., 2016).

Structural, vibrational, and electronic properties were investigated by means of periodic first-principles calculations in the framework of density functional theory (DFT) with the B3LYP hybrid functional (Lee, Yang and Parr, 1988; Becke, 1993) using the CRYSTAL 17 package (Dovesi et al, 2017; Erba et al., 2017). The Grimme D3 potential (Grimme et al., 2010) was included to correct dispersion interactions, which may improve the structural and vibrational description. B3LYP functional has been successfully employed to describe many properties in several strongly correlated systems, serving as reference on the computational calculations of solids in periodic systems (Longo et al., 2014). CRYSTAL 17 program uses

Gaussian-type basis set to represent crystalline orbitals as a linear combination of Bloch functions defined in terms of local functions. The all-electron triple-zeta 6211/411/1 (*s*/*p*/*d*) basis set was used for oxygens, and the Hay and Wadt small core (HAYWSC) pseudopotentials 311/31 (*sp*/*d*) for Ag and Mo, as available within the Crystal Basis Set Library (Dovesi et al., 2017). The β-Ag_2MoO_4 is a closed-shell system and was treated under restricted Kohn-Sham formalism. The accuracy for the Coulomb and exchange series was controlled by five tight thresholds parameters set to (10^{-10}, 10^{-10}, 10^{-10}, 10^{-10}, 10^{-20}). The shrinking factor (Pack–Monkhorst and Gilat net) was set to 4, corresponding to 40 independent *k*-points in the irreducible part of the Brillouin zone integration in the primitive cell.

The SCF criteria convergence was governed by a threshold on energy of 10^{-10} and 10^{-11} Hartree for geometry optimizations and vibrational calculations, respectively. All structures were fully optimized (atomic positions and lattice parameters) with the Broyden-Fletcher-Goldfarb-Shanno (BFGS) algorithm for Hessian updating, taking very tight criteria for convergence on gradient (0.0001 a.u.) and nuclear displacements (0.0004 a.u.).

Infrared and Raman normal modes and their correspondent harmonic frequencies were obtained from tightly optimized bulks. The frequencies were computed at the *G* point by diagonalizing the mass-weighted Hessian matrix. The Raman spectra with relative intensities of the peaks were computed analytically by exploiting a scheme based on the solution of first- and second-order Coupled-Perturbed-Hartree-Fock/Kohn-Sham (CPHF/KS) equations (Ferrero et al., 2008a,b), recently implemented in CRYSTAL. To the best of our knowledge, this is the first report describing the Raman spectra of β-Ag_2MoO_4 in this way. The code enables to simulate the final spectrum of powder samples taking into account all possible orientations of solid, providing a fingerprint by which the contribution of each cluster vibration can be detailed described. The modes were visualized through J-ICE program (Canepa et al., 2011).

The electronic structure was studied through atomic charges, band structure and its density of states (DOS), analyzed using the Properties 17 routine of the CRYSTAL code, considering the same k-point sampling as that used during the diagonalization of the Fock matrix. Electronic band structure was obtained at the appropriate high-symmetry path in the first Brillouin zone, and the density of states (DOS) was calculated according to the Fourier-Legendre technique, with polynomial degree equal to 12.

3. Results and discussion

3.1. XRD, Rietveld refinement data, XRF and unit cell representation of β-Ag_2MoO_4 crystals analysis

The degree of structural order-disorder at long-range or the periodicity of crystalline lattice for β-Ag_2MoO_4 microcrystals was verified by the XRD technique. Fig. 1(a) and (b) shows XRD patterns of β-Ag_2MoO_4 microcrystals prepared at different temperatures (100, 120, 140 and 160 °C) for 2 h by the CH method and illustrates theoretical XRD profile with their specific lines position of the optimized cubic structure, respectively.

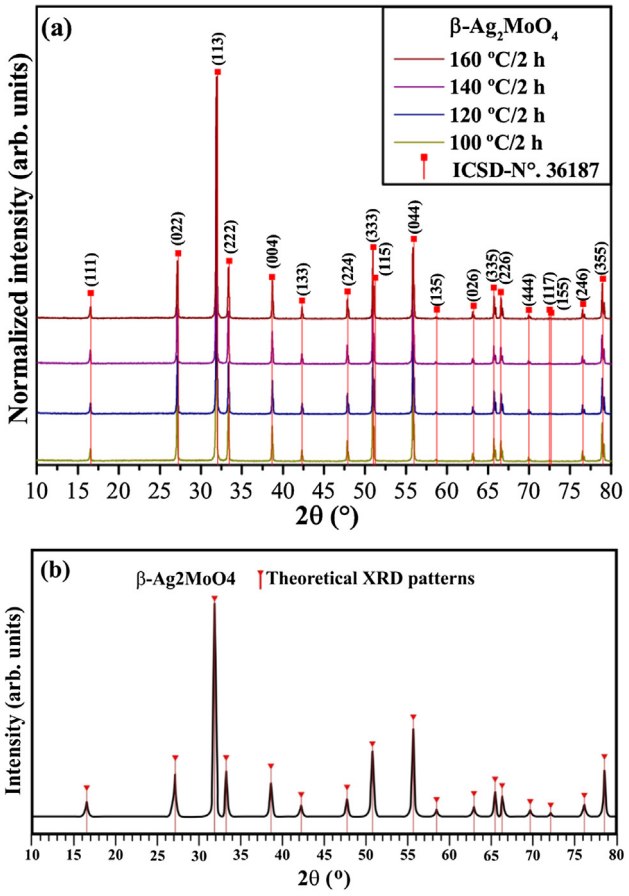

Fig. 1 (a) XRD patterns of β-Ag_2MoO_4 microcrystals synthesized by the CH method at different temperatures (100, 120, 140 and 160 °C) for 2 h and (b) XRD patterns theoretically calculated, respectively. The vertical red lines indicate the position and relative intensity of the respective ICSD Card N°. 36187.

According to the XRD patterns analysis illustrated (Fig. 1a), all XRD peaks can be indexed perfectly to a spinel-type cubic structure with the space group ($Fd\bar{3}'m$) and point-group symmetry (O_h^7) (Wyckoff, 1992; Cunha et al., 2015). These crystals have sharp and well-defined diffraction peaks with a good degree of structural order at long range, and any diffraction peaks were observed to silver oxide (Ag_2O) or reduced silver (Ag^0) nanoparticles by means of XRD measurements (Cavalcante et al., 2012a,b,c,d). Moreover, respective positions of all diffraction peaks in these XRD diffractograms are in good agreement with results reported in the Inorganic Crystal Structure Data (ICSD) base N°. 36187 (Wyckoff, 1922) and the literature (Cao et al., 2017; Zhang & Ma, 2017a,b). The experimental lattice parameters, unit cell volume and atomic positions of β-Ag_2MoO_4 microcrystals were calculated using the Rietveld refinement method (Rietveld, 1967) with the FULLPROF software version 2016 (Rodriguez-Carvajal 2010, Som & Sharma, 2012). The experimental results obtained from Rietveld refinement were optimized by theoretical calculations. The theoretical lattice parameters and atomic positions were used to model theoretical XRD profile with their specific lines position (Fig. 1b).

Structural refinements using the Rietveld method (Rietveld, 1967) confirmed that all β-Ag_2MoO_4 microcrystals have a

spinel-type cubic structure without secondary phases (see Fig. 2a–d).

From the standard diffraction data obtained by the XRD characterization, as well as the information extracted from the ICSD Card N°. 36187, a more detailed study of the microstructures was made using the Rietveld method (Araújo Júnior et al., 2017). In Fig. 2(a)–(d) and Table 1, we find the information experimental extracted from the structural refinement and theoretical obtained ly calculated from DFT. The Rietveld refinement data are consisted in evaluating the agreement of the lattice parameters and internal angles (a, b, c, α, β and γ), unit cell volume (V) observed parameters (Y_{Obs}), calculated parameters (Y_{Cal}) for the residual line profile ($Y_{Obs} - Y_{Cal}$) and the R-parameters of (R_{exp}, R_{wp}, R_b,χ^2 and S), using the free availability software Fullprof, July 2016 version (Som & Sharma, 2012).

The X-ray fluorescence (XRF) data is shown in Table 1, which was used to verify the percentage composition of metals silver (Ag) and molybdenum (Mo) in β-Ag_2MoO_4 microcrystals synthesized at different temperatures by the CH method for 2 h, showing that the percentages of silver (Ag = 60%) and molybdenum (Mo = 40%) did not undergo stoichiometric variations of these in the composition.

The experimental, theoretical and residual graphic profile implied a good quality of the structural refinement, corroborating with the pertinent information to the parameters R in good concordance (see Table 1) presents a good agreement with the percentage composition of the metals employed indicating that no leaching occurred during the CH synthesis. The atomic coordinates (x, y. and z) of the silver (Ag) and molybdenum (W) atoms did not result in significant variations in their positions in the unit cell, remaining fixed in the same ones arranged in ICSD Card N°. 36187. However, the atomic positions for the present oxygen atoms have undergone considerable variations, resulting from a high degree of distortions of the octahedral [AgO_6] clusters, tetrahedral [MoO_4] clusters, strain, oxygen atom vacancy (V_0^x) as a function of nucleation process and growth of β-Ag_2MoO_4 microcrystals by the CH method employed (Gouveia et al., 2014).

The average size of the microcrystals (D'_{hkl}) was calculated using the Debye-Scherrer equation (Bindu & Thomas, 2014)

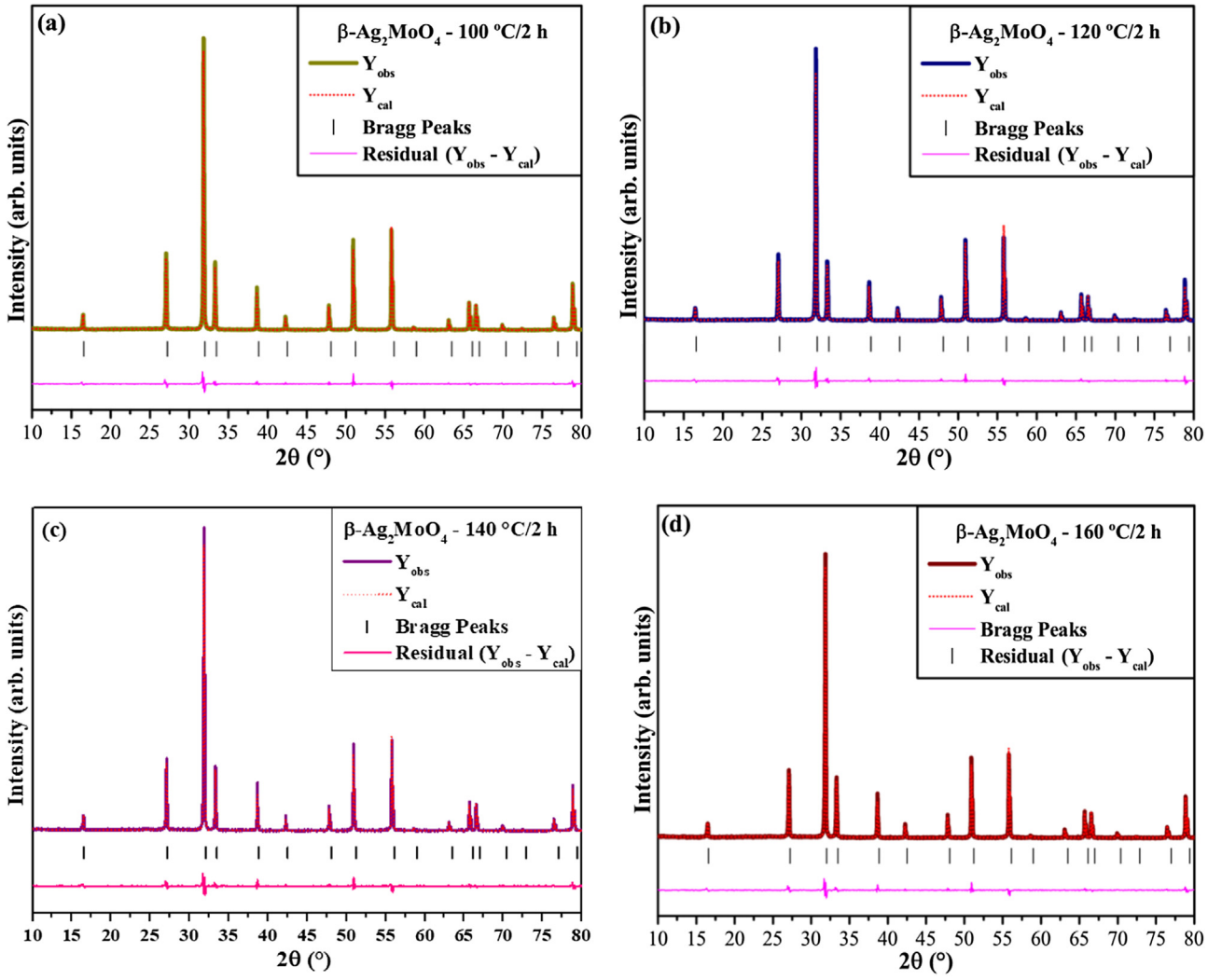

Fig. 2 Rietveld refinement plot for β-Ag_2MoO_4 microcrystals synthesized by the CH method at different temperatures: (a) 100 °C, (b) 120 °C, (c) 140 °C and (d) 160 °C for 2 h, respectively.

Table 1 Correlation between Rietveld refinaments results of lattice parameters ($a = b = c$), atomic coordinates (x, y, and z), sites, unit cell volume (V), $R_{paraments}$ (R_p, R_{wp}, R_{exp}, χ^2 and S) for β-Ag_2MoO_4 microcrystals synthesized at different temperatures: (a) 100 °C, (b) 120 °C, (c) 140 °C, (d) 160 °C and (e) theoretical calculations and references rerpoted in the literature and.

[(a)]Atoms	Wyckoff	Site	Atomic coordinated			X_{atom} (%)	V (Å^3)
			x	y	z		
Ag	16*d*	.−3m	0.62500	0.62500	0.62500	60	807.92(8)
Mo	8*a*	−43 m	0	0	0	40	
O	32*e*	.3m	0.26867	0.26867	0.26867	–	
Refined parameters: $a = b = c = 9.313(7)$ Å, $\alpha = \beta = \gamma = 90°$, $R_p = 22.6\%$, $R_{wp} = 22.8\%$, $R_e = 15.7\%$, $\chi^2 = 2.1$ and $S = 1.4$.							
[(b)]Atoms	Wyckoff	Site	Atomic coordinated			X_{atom} (%)	V (Å^3)
			x	y	z		
Ag	16*d*	.−3m	0.62500	0.62500	0.62500	60	
Mo	8*a*	−43 m	0	0	0	40	808.24(6)
O	32*e*	.3m	0.26965	0.26965	0.26965	–	
Refined parameters: $a = b = c = 9.3150(7)$ Å, $\alpha = \beta = \gamma = 90°$, $R_p = 23.0\%$, $R_{wp} = 23.5\%$, $R_e = 16.3\%$, $\chi^2 = 2.0$ and $S = 1.4$.							
[(c)]Atoms	Wyckoff	Site	Atomic coordinated			X_{atom} (%)	V (Å^3)
			x	y	z		
Ag	16*d*	.−3m	0.62500	0.62500	0.62500	60	
Mo	8*a*	−43 m	0	0	0	40	808.06(4)
O	32*e*	.3m	0.26841	0.26841	0.26841	–	
Refined parameters: $a = b = c = 9.314(3)$ Å, $\alpha = \beta = \gamma = 90°$, $R_p = 23.2\%$, $R_{wp} = 23.8\%$, $R_e = 16.4\%$, $\chi^2 = 2.1$ and $S = 1.4$.							
[(d)]Atoms	Wyckoff	Site	Atomic coordinated			X_{atom} (%)	V (Å^3)
			x	y	z		
Ag	16*d*	.−3m	0.62500	0.62500	0.62500	60	
Mo	8*a*	−43 m	0	0	0	40	808.08(6)
O	32*e*	.3m	0.26991	0.26991	0.26991	–	
Refined parameters: $a = b = c = 9.314(2)$ Å, $\alpha = \beta = \gamma = 90°$, $R_p = 23.0\%$, $R_{wp} = 23.0\%$, $R_e = 16.6\%$, $\chi^2 = 1.9$ and $S = 1.3$.							
[(e)]Atoms	Wyckoff	Site	Atomic coordinated			X_{atom} (%)	V (Å^3)
			x	y	z		
Ag	16*d*	.−3m	−0.375	−0.125	−0.125	–	
Mo	8*a*	−43 m	0	0	0	–	816.19(4)
O	32*e*	.3m	0.36108	−0.13892	−0.13892	–	
Refined parameters: $a = b = c = 9.35(4)$ Å, $\alpha = \beta = \gamma = 90°$.							

(a) = Ag_2MoO_4 – 100 °C, (b) = Ag_2MoO_4 – 120 °C, (c) = Ag_2MoO_4 – 140 °C, (d) = Ag_2MoO_4 – 160 °C, (e) = Ag_2MoO_4 (Theoretically calculated from DFT method), V = volume of unit cell and X_{atom} = atomic percent by XRF analysis of metals (Mo and Ag).

presented in Eq. (4), where k corresponds to a constant related to the crystalline structure, being attributed to the present study $k = 0.9$ (approximately spherical) since silver molybdate (β-Ag_2MoO_4) microcrystals exhibit cubic structure, and λ is the wavelength of the radiation used in the measurement (Cu-Kα, λ = 0.1540 nm).

$$D_{hkl} = \frac{k\lambda}{\beta_{hkl}\cos\theta} \tag{4}$$

In the presented equation, β_{hkl} is corresponds to the full width at half height (FWHM) for the corrected diffraction planes, obtained by Eq. (5), where β_{sample} refers to FWHM of the diffraction peaks of the samples and $\beta_{instrumental}$ to FWHM obtained from the diffraction pattern and Rietveld's refinement, in this work, pure silicon.

$$\beta_{hkl} = \left[(\beta_{sample})^2 - (\beta_{instrumental})^2\right]^{1/2} \tag{5}$$

The results obtained using the Eqs. (4) and (5) for the microcrystals synthesized at 100, 120, 140 and 160 °C are 99.606(4), 96.808(4), 99.123(4) and 94.285(2) nm, respectively.

As it can be noted, no linearity of the average microcrystals size was observed with the raise in hydrothermal synthesis temperature for 2 h. However, it was verified an increase in the volume of the unit cell (V), when the synthesis temperature was raised from 100 to 120 °C and from 120 to 140 °C. On the other hand, there was a decrease in average crystals size at temperatures from 140 to 160 °C.

Fig. 3(a) and (b) illustrates a schematic representation of a cubic unit cell for β-Ag_2MoO_4 structure modeled from Rietveld refinement data and structure modeled from theoretical calculations, respectively.

Lattice parameters and atomic positions obtained from Rietveld refinements were used to model this structure by the Visualization for Electronic and Structural Analysis (VESTA) program (version 3.4.0 for Windows) (Momma & Izumi,

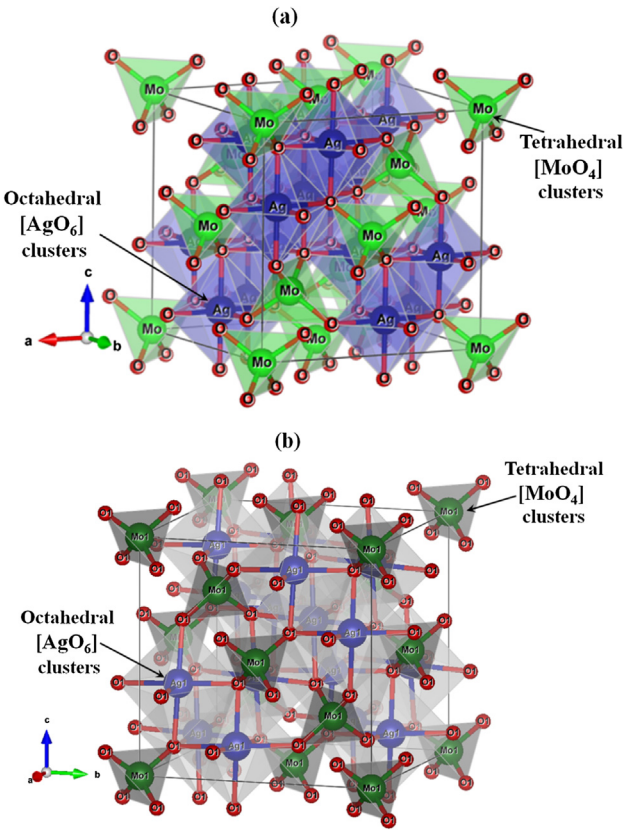

Fig. 3 Schematic representation of the cubic unit cells corresponding to β-Ag_2MoO_4 microcrystals projected at same axis: (a) experimental and (a) theoretical, respectively.

2011). The spinel-type cubic structure of β-Ag_2MoO_4 microcrystals is characterized by the space group ($Fd\bar{3}'m$) with eight molecular formula per unit cell (Z = 8) (Wyckoff, 1992). In these structures, silver atoms are coordinated to six oxygen atoms which form distorted octahedral [AgO_6] clusters. These polyhedra have a symmetry group (O_h) with six vertices, eight faces and twelve-edges (Cunha et al., 2015) (see Fig. 3a and b). In this same figure, molybdenum atoms are coordinated to four oxygen atoms which result in tetrahedral [MoO_4] clusters. In this case, these tetrahedra are related to the T_d symmetry group with four vertices, four faces and six edges (Cunha et al., 2015). These [MoO_4] clusters are slightly distorted in the lattice and exhibit a particular characteristic related to differences in O—Mo—O bond angles. These characteristics presented by these β-Ag_2MoO_4 microcrystals obtained at different temperatures present direct relations with the crystalline defects and interatomic distances caused by the distortions in the angles between the chemical bonds (Mo—O—Mo), (Ag—O—Ag) or (Mo—O—Ag) presents into the crystalline lattice. Moreover, it was verified an increase in the unit cell volume (Table 1) as a function of crystal growth mechanism with the modifications in the thermodynamic variables (temperature and pressure). In our case, the intrinsic defects can be increased with the temperature rise. Therefore, we presume that experimental conditions employed in the synthesis as well as the influence of the hydrothermal processing to crystals growth are key factors which caused local distortions in both octahedral [AgO_6] and tetrahedral [MoO_4] clusters.

3.2. Experimental and theoretical micro-Raman and infrared spectroscopy analysis

β-Ag_2MoO_4 microcrystals obtained in this work exhibit a spinel-type cubic structure with a space group ($Fd\bar{3}'m$), a point-group symmetry (O_h^7) and eight molecules per unit cell (Z = 8) (Wyckoff, 1992). According to group theory calculations, β-Ag_2MoO_4 microcrystals exhibits a total irreducible representation of vibrational modes or optical phonons is shown in Brillouin zone points as described by Eq. (6) (Beltrán et al., 2014):

$$\Gamma_{\{[\text{Raman}]+(\text{Infrared})\}} = \{[A_{1g} + E_g + 3T_{2g} + T_{1g}] + (2A_{2u} + 2E_u + 2T_{2u} + 4T_{1u})\} \quad (6)$$

where A_g, E_g, and $3T_{2g}$ are Raman-active modes, while the T_{1g} mode has a very low intensity and is considered inactive. The $4T_{1u}$ are Infrared-active modes and, $1T_{1u}$ is Infrared-acoustic modes. However, it is very difficult to be detected all $4T_{1u}$ modes in our infrared spectrometers, and the other ($2A_{2u}$ + $2E_u$ + $2T_{2u}$ + $4T_{1u}$) are Hyper-Raman active modes or Acoustic modes not included. The subscript terms "$_g$" and "$_u$" indicate that the β-Ag_2MoO_4 phase has a centrosymmetric inversion. Therefore, only five active vibrational modes are expected in β-Ag_2MoO_4 crystal Raman spectra as represented by Eq. (7):

$$\Gamma_{[\text{Raman}]} = [A_{1g} + E_g + 3T_{2g}] \quad (7)$$

Fig. 4(a) shows the m-Raman spectra of β-Ag_2MoO_4 microcrystals prepared at different temperatures for 1 h by the CH method, Fig. 4(b) illustrates theoretical Raman spectrum with their specific lines position of optimized cubic structure and Fig. 4(c) is illustrated the experimental and theoretical positions of these Raman-active vibrational modes, respectively.

In m-Raman spectra displayed in Fig. 4(a) were identified five Raman-active modes located between 50 cm^{-1} and 1000 cm^{-1}. All these Raman modes are intense and well defined, it is possible to conclude that all β-Ag_2MoO_4 microcrystals are structurally ordered at short-range, and there are no active modes related to secondary phases, corroborating with the information obtained by DRX patterns and Rietveld refinement data (see Figs. 1a and 2a–d). The T_{2g} mode located at 86 cm^{-1} is due to external modes of oxygen atoms with symmetric bending vibrations presents in tetrahedral [MoO_4] clusters. The E_g mode located at 277 cm^{-1} is due to external structure vibrations of octahedral [AgO_6] clusters, while T_{2g} modes found at 353 cm^{-1} and 761 cm^{-1} are related to torsional vibrations of oxygen atoms and molybdenum atoms in O—Mo—O bonds inside tetrahedral [MoO_4] clusters. The A_{1g} mode situated at 872/873 cm^{-1} is ascribed to symmetric stretching vibrations of oxygen atoms in [←O ← Mo → O→] bonds (Gouveia et al., 2014; Moura et al., 2017; Kroumova et al., 2003; Zhou et al., 2017).

The computational theoretical study of the frequencies and intensity of the Raman-active modes for the microcrystals of β-Ag_2MoO_4 was performed at the DFT/B3LYP-D3 level for solving the equations of first and second order (Coupled-Perturbed-Hartree-Fock/Kohn-Sham, CPHF/KS) to obtain the theoretical Raman spectrum shown in Fig. 4(b). Moreover, the relative experimental and theoretical positions of these vibrational modes displayed in Fig. 4(c) indicates a good

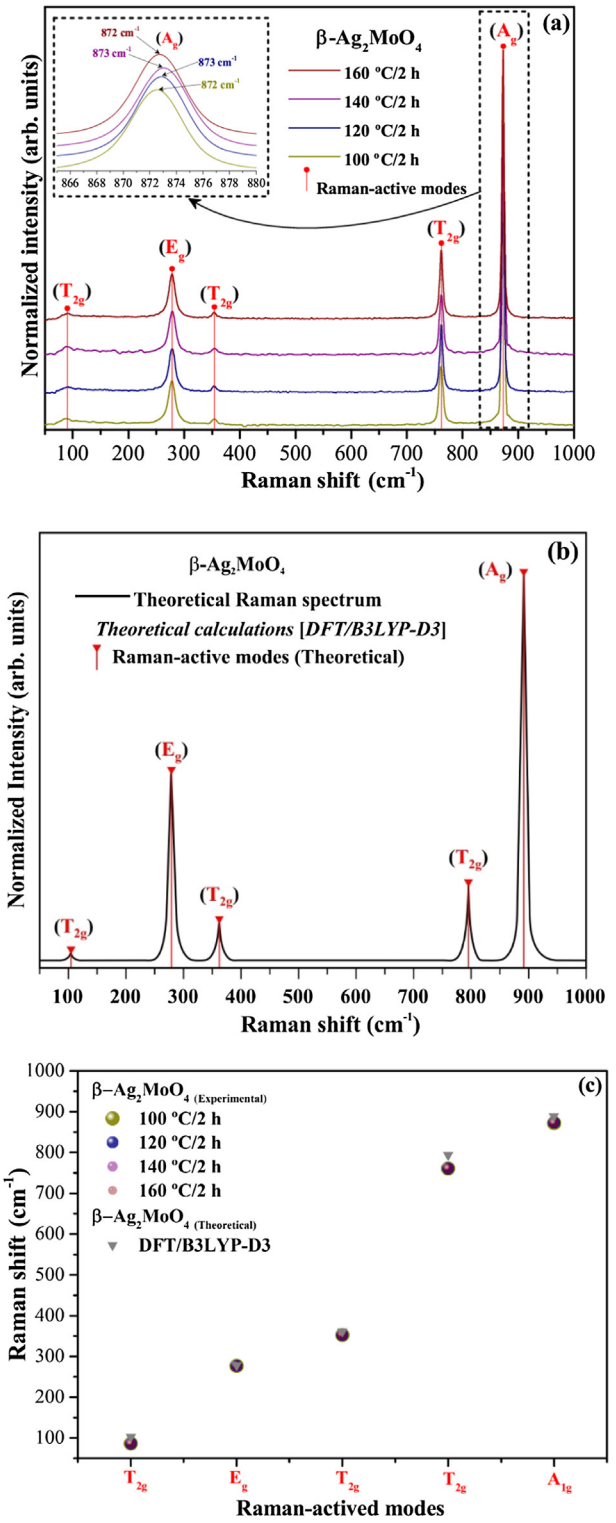

Fig. 4 (a) m-Raman spectra experimental from 50 to 1000 cm^{-1} of β-Ag_2MoO_4 microcrystals obtained by the hydrothermal method at different temperatures for 2 h, (b) Theoretical Raman spectrum by DFT/B3LYP-D3 and (c) Comparing of position of the experimental and theoretical Raman-active modes. The vertical lines indicate the positions of the experimental/experimental Raman modes.

agreement between experimental and theoretical Raman modes of β-Ag_2MoO_4 microcrystals.

The Table 2 presents show a comparative between the relative positions of Raman-active modes for the β-Ag_2MoO_4 microcrystals in this work with those reported in the literature (Gouveia et al., 2014; Moura et al., 2017; Zhou et al., 2017).

A detailed analysis of the results reported in Table 2 revealed some small variations in the relative positions corresponding to the Raman-active modes. In fact, it is acceptable that the presence of defects at short-range, interaction force between the clusters as well as the degree of structural order-disorder into the lattice can be responsible for this behavior.

Fig. 5(a) shows FT-IR spectra in the range from 400 to 11,000 cm^{-1} of β-Ag_2MoO_4 microcrystals prepared at different temperatures for 1 h by the CH method and Fig. 5(b) is illustrated the experimental and theoretical positions of these IR-active vibrational modes, respectively.

In infrared spectra are expected ten infrared vibrational modes for β-Ag_2MoO_4 crystals, excluding the six Raman vibrational modes, as presented in Eq. (8) (Gouveia et al., 2014; Moura et al., 2017; Zhou et al., 2017):

$$\Gamma_{(\text{Infrared})} = (2A_{2u} + 2E_u + 2T_{2u} + 4T_{1u}) \quad (8)$$

However, the $2A_{2u}$, $2E_u$ and $2T_{2u}$ are acoustic vibrations modes, i.e., infrared-inactive modes, while the others $4T_{1u}$ IR-active vibrational modes. Therefore, only 4 infrared-active vibrational modes remain, as presented in Eq. (9) (Gouveia et al., 2014; Moura et al., 2017; Kroumova et al., 2003; Zhou et al., 2017).

$$\Gamma_{(\text{Infrared})} = 4T_{1u} \quad (9)$$

In our FT-IR spectra illustrated in Fig. 5(a), only one of the four IR-active modes were verified. The $1T_{1u}$ modes may not have been detected due to limitations imposed by the FT-IR equipment. As was previously described, the β-Ag_2MoO_4 crystals with spinel-type cubic structure with four stretching and bending vibrational modes. The IR-active modes related to $1T_{1u}$ located at 834 cm^{-1} is ascribed to anti-symmetric stretch (→O → Mo → O→) of distorted tetrahedral [MoO_4] clusters. Typical theoretical (★) and experimental positions (◆) of IR-active modes are shown in Fig. 5(b). Moreover, their respective experimental and theoretical IR-active modes values are listed in Table 3 and compared to those values already reported in the literature.

This table verifies that some IR-active-mode relative positions have small shifts, which can be caused by different factors such as the preparation methods, average crystal size, distortions on O—Mo—O/O—Ag—O bonds, interaction forces between [AgO_6]–[MoO_4] clusters, and/or different degrees of structural order-disorder in the lattice at short range (Gouveia et al., 2014; Moura et al., 2017; Zhou et al., 2017).

3.3. UV–vis diffuse reflectance spectroscopy of β-Ag_2MoO_4 microcrystals

The optical band gap energy (E_{gap}) was calculated by the Kubelka-Munk equation (Kubelka and Munk, 1931) which is based on the transformation of diffuse reflectance measurements to estimate E_{gap} values with good accuracy (Morales

Table 2 Experimental and theoretical relative position of Raman-active vibrational modes for β-Ag_2MoO_4 microcrystals compared with those reported in the literature.

Methods	Temperature (°C)	Raman active modes					Ref.
		T_{2g}	E_g	T_{2g}	T_{2g}	A_{1g}	
This work	100	86	277	353	761	872	⊗
	120	86	277	353	761	873	⊗
	140	86	277	353	761	873	⊗
	160	86	277	353	761	872	⊗
Theoretical $_{(DFT/B3LYP-D3)}$	–	102	278	361	794	889	
MH	140	–	277	348	756	867	✙
PC	300	102	296	372	779	893	♠
HC	160	91	277	353	761	873	✠

Legend: ⊗ = this work.

✙ = Moura et al. (2017); ♠ = Fabro et al., 2015;

✠ = Moura et al. (2016).

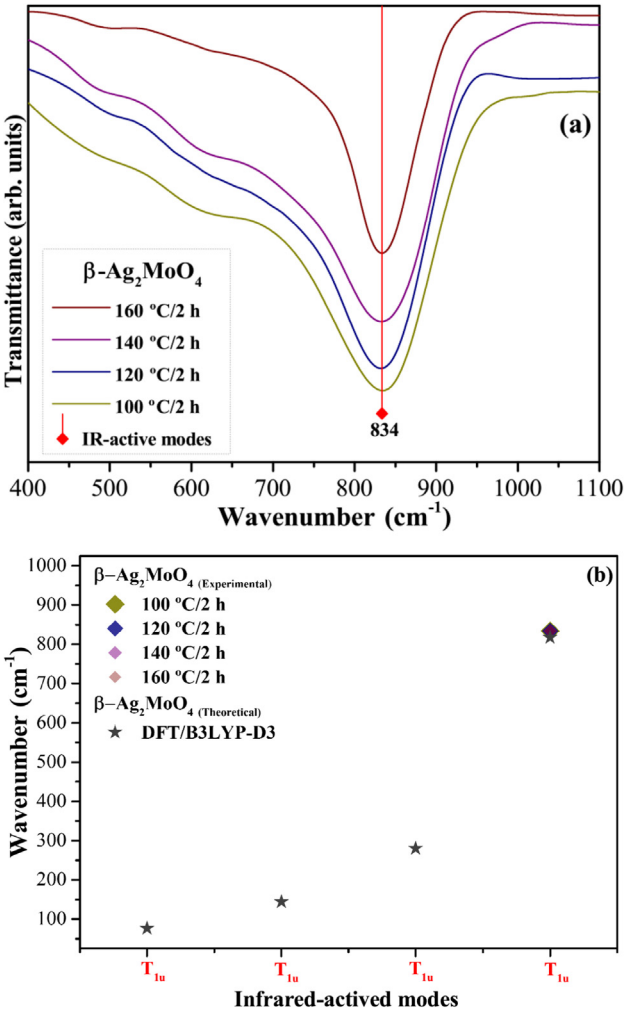

Fig. 5 (a) FT-IR spectra experimental from 400 to 1100 cm^{-1} of β-Ag_2MoO_4 microcrystals obtained by the hydrothermal method at different temperatures for 2 h, and (b) Comparing of position of the experimental and theoretical IR-active modes. The vertical lines indicate the positions of the experimental/experimental IR modes.

et al., 2007). Particularly, it is used in limited cases of infinitely thick samples. The Kubelka–Munk Eq. (10) for any wavelength is described by:

$$F(R_\infty) = \frac{(1 - R_\infty)^2}{2R_\infty} = \frac{k}{s} \tag{10}$$

where $F(R_\infty)$ is the Kubelka–Munk function or absolute reflectance of the sample. In our case, barium sulfate ($BaSO_4$) was adopted as the standard sample in reflectance measurements; $R_\infty = R_{sample}/R_{BaSO4}$ (R_∞ is the reflectance), k is the molar absorption coefficient, and s is the scattering coefficient. In a parabolic band structure, the optical band gap and absorption coefficient of semiconductor oxides (Smith, 1978) can be calculated by eq. (11):

$$\alpha h\nu = C_1 \tag{11}$$

where α is the linear absorption coefficient of the material, hν is the photon energy, C_1 is a proportionality constant, E_{gap} is the optical band gap and n is a constant associated with different kinds of electronic transitions (n = 0.5 for a direct allowed, n = 2 for an indirect allowed, n = 1.5 for a direct forbidden and n = 3 for an indirect forbidden). According to our theoretical calculations, β-Ag_2MoO_4 microcrystals exhibit an optical absorption spectrum governed by indirect electronic transitions. In this phenomenon, after the electronic absorption process, electrons located in minimum energy states in the conduction band (CB) are able to go back to maximum energy states of the valence band (VB) in distinct points in the Brillouin zone (Gouveia et al., 2014; Lacomba-Perales et al., 2008). Based on this information, E_{gap} values of β-Ag_2MoO_4 microcrystals were calculated using n = 2 in Eq. (11). Finally, using the absolute reflectance function described in Eq. (10) with k = 2α, we obtain the modified Kubelka–Munk equation as indicated in:

$$[F(R_\infty h\nu)]^n = C_2(h\nu - E_{gap}) \tag{12}$$

Therefore, finding the $F(R_\infty)$ value from and plotting a graph of $[F(R_\infty)h\nu]^2$ against hν, E_{gap} values were calculated for β-Ag_2MoO_4 microcrystals by extrapolating the linear portion of UV–vis curves.

Fig. 6(a)–(d) illustrate UV–vis spectra of β-Ag_2MoO_4 microcrystals prepared at different temperatures by the CH

Table 3 Comparative results between the experimental and theoretical IR-active modes of β-Ag_2MoO_4 microcrystals obtained in this work with those published in the literature.

Methods	Temperature (°C)	Raman active modes					Ref.
		F_{1u}	F_{1u}	F_{1u}	F_{1u}	F_{1u}	
This work	100					834	⊗
	120					834	⊗
	140					834	⊗
	160					834	⊗
Theoretical $_{(DFT/B3LYP-D3)}$		0	76	144	280	817	⊗
CH	120					891	⊕

Legend: CH = Conventional hydrothermal ⊗ = this work.

⊕ = Kumar et al. (2016).

method, and the optical band gap values obtained as a function of processing temperature are shown in Fig. 6(e), respectively.

The E_{gap} is of fundamental importance in the discussions about orders/disorders, crystalline defects and vacancies in the long, medium and short range in the crystalline structures, implying the optical and catalytic properties. From the E_{gap} values, it becomes possible to establish the photon energy (hν), i.e. the wavelength of the radiation to be used to excite electrons from the VB) to the CB. Since that the photon energy must be of magnitude equal to or greater than the energy of $E_{gap} - h\nu \geq E_{gap}$ (Mith and Nie, 2010).

As it can be observed in Fig. 6(a)–(e), its noted a slight decrease in the E_{gap} values with an increase in the processing temperature. In principle, we believe that this behavior is related to the appearance of intermediary energy levels between the VB and CB, since the exponential optical absorption edge and E_{gap} are controlled by the degree of structural order-disorder in the lattice (Cavalcante et al., 2012a,b,c,d). The decrease in E_{gap} values can be attributed to structural defects at medium range and local bond distortions which yield localized electronic levels within the forbidden band gap (Cavalcante et al., 2013). A smaller E_{gap} was detected for β-Ag_2MoO_4 microcrystals processed at 160 °C for 2 h (see Fig. 6a) which suggests a high concentration of defects in the lattice due to high temperature employed in hydrothermal synthesis (Cavalcante et al., 2012a,b,c,d). Moreover, the obtained results and illustrated in Fig. 6(e) are listed in Table 4.

As it can be noted in this table the comparative between the E_{gap} values of β-Ag_2MoO_4 microcrystals obtained in this work and theoretically calculated by the DFT method and those reported in the literature exhibit a very good agreement. However, the presence of k-points between the VB and CB and electronic levels in these crystals can be achieved only by theoretical calculations, which will be shown below.

3.4. Band structures, density of states and map of charge density for β-Ag_2MoO_4 crystals

The lattice parameters (a = 9.345 Å; V = 816.2 $Å^3$) and atomic positions of β-Ag_2MoO_4 crystals were obtained in close agreement with experimental data. An accurate description of structural parameters is the first step to obtain reliable results on frequencies and electronic structure.

As it can be observed in Fig. 7(a), is shown the electronic band structure have revealed an indirect band gap ($\Gamma \leftarrow X$) = 3.94 eV, close to experimental value, and similar to previous studies (Gouveia et al., 2014) using plane waves basis set. The lower direct ($\Gamma \leftarrow \Gamma$) transition is 4.04 eV. It is well described that optical gaps can be empirically adjusted by modifying the amount of exact Hartree-Fock exchange included in the hybrid functional, although this may also worsen the description of the reduced cations. Besides, it should lead to results similar to those obtained with the more sophisticated, but still semiempirical, hybrid functional approach.

Fig. 7(a) and (b) illustrate the electronic band structure, and density of states for β-Ag_2MoO_4 crystals which were theoretically calculated from DFT method, respectively.

It is well described that optical gaps can be empirically adjusted by modifying the amount of exact Hartree-Fock exchange included in the hybrid functional, although this may also worsen the description of the reduced cations. Besides, it should lead to results similar to those obtained with the more sophisticated, but still semiempirical, hybrid functional approach. The density of states (DOS) projected on each atom is displayed in Fig. 7(b) and indicates an edge of the valence band (VB) composed mainly by Ag and O atoms, while the bottom of conduction band (CB) is composed by Ag, Mo and O atoms. The Fermi level is located at -5.26 eV, between the redox potential of H^+/H_2 and O_2/H_2O. Any local disorder on O—Mo—O or O—Ag—O bond length or angles, originated by local stress, or edge and interfaces deformation are sufficient to break the symmetry of clusters and modify the band gap. If the local disorder is already present before light radiation, the polaronic deformation is facilitated and the material should present a better photocatalytic activity than the perfect single crystal. It is only one factor that can determine the generation of electrons (e′)/holes ($h^{\bullet}$) pair. The crystalline orbitals related to the top of VB are hybridized Ag 4*d* orbitals and O 2*p* orbitals, while the bottom of CB is formed by Mo 4*d* orbitals and O 2*p* orbitals (Gouveia et al., 2014).

Fig. 8 shows the charge density difference ($\rho_{solid} - \rho_{atom}$) on three selected planes across the O —Mo—O, O—Ag—O and Ag—Ag bonds.

The Mulliken electron distribution analysis reinforces the structural point of view in which the tetrahedral [MoO_4] clusters form chemical bonds more covalent than Ag—O bonds, which form the octahedral [AgO_6] clusters. Blue and red

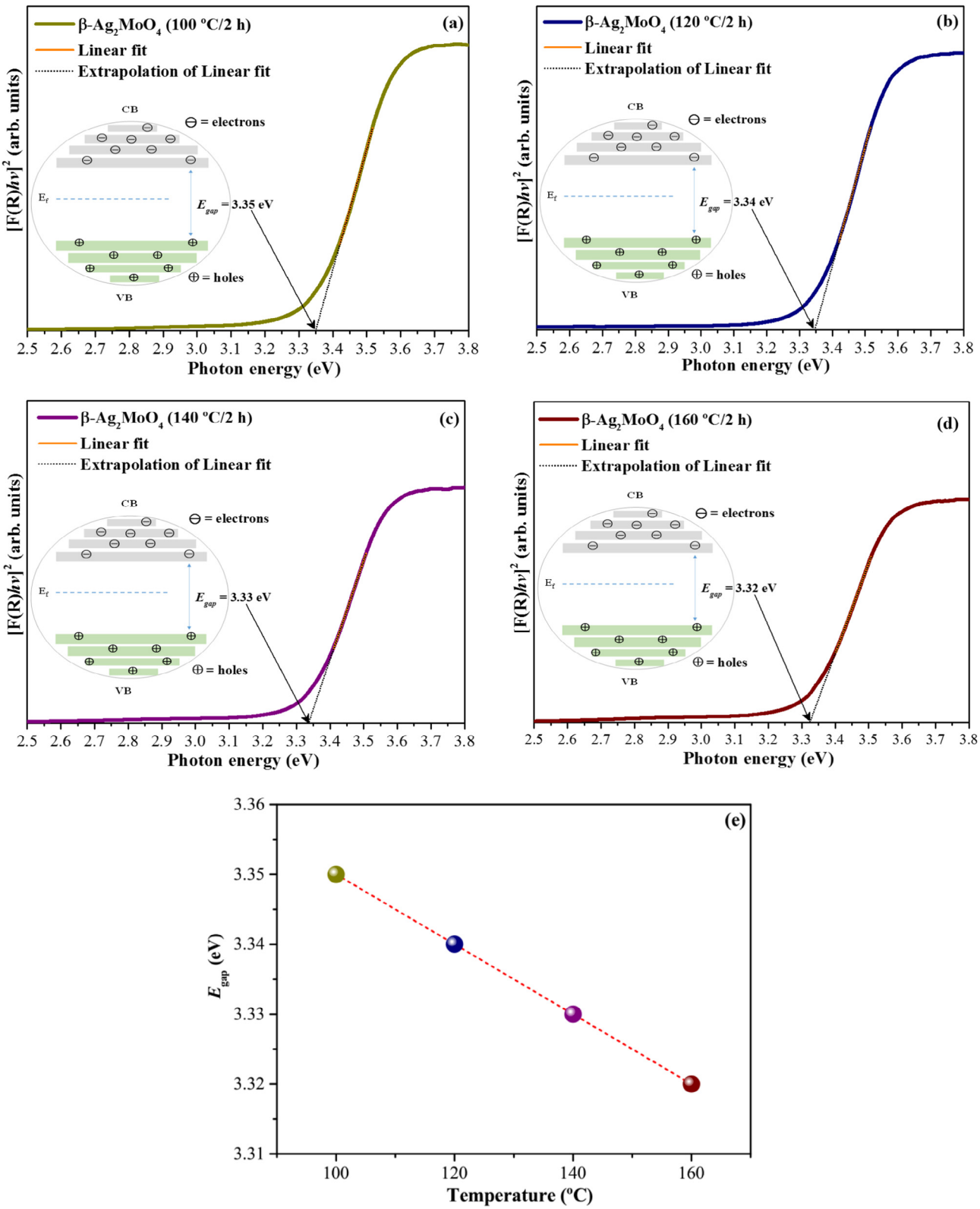

Fig. 6 UV–vis absorbance spectra of β-Ag_2MoO_4 microcrystals synthesized by CH method at different temperatures: (a) 100 °C, (b) 120 °C, (c) 140 °C, (d) 160 °C for 2 h and (e) optical band gap (E_{gap}) values as a function of temperature.

regions on maps show the loss and gain of electron, respectively, concerning isolated atom, exposing clearly the effect of the solid environment as shown in Fig. 8. Besides charge maps, the Mulliken atomic charges point out the fluctuation local in the electron density and electronic polarization on the metal-oxygen bonds.

Table 4 Comparative results of the optical band gap energy (E_{gap}) values of β-Ag_2MoO_4 microcrystals obtained in this work with those reported in the literature.

Methods	Temperature (°C)	Time (min)	E_{gap} (eV)	Ref.
This work	100	120	3.31	⊗
	120	120	3.30	⊗
	140	120	3.29	⊗
	160	120	3.26	⊗
MAH	60	480	3.32	✟
CP	90	10	3.32	♠
CH	160	60	3.31	✠

Legend: MAH = Microwave-Assisted Hydrothermal; CP = Controlled Precipitation; CH = Conventional hydrothermal; ⊗ = this work; ✟ = Cunha et al., 2015; ♠ = Fabbro et al., 2016; ✠ = Gouveia et al., 2014.

3.5. FE-SEM images and growth process analyses of β-Ag_2MoO_4 microcrystals

Fig. 9(a)–(l) illustrate FE-SEM images of β-Ag_2MoO_4 microcrystals prepared at different temperatures: (a)–(c) 100 °C, (d)–(f) 120 °C (g)–(i) 140 °C and (j)–(l) 160 °C for 2 h by the CH method, respectively.

In CH processing stages at 100 °C for 2 h, the growth is promoted by interior part of the furnace through the thermal energy. In this case, the electrical resistances provide the thermal energy transferred to suspension, which the starting β-Ag_2MoO_4 microcrystals from aqueous of their respective starting salts to accelerate solid particles to high velocities. These two phenomena induce a random aggregation between the small particles due to the increase in effective collisions which results in a system composed of several irregular β-Ag_2MoO_4 microcrystals (see Fig. 9a–c). The FE-SEM images illustrated in Fig. 9(c)–(i) confirms a mass transport between these particles in contact at temperatures of 120 °C and 140 °C, respectively. As a consequence of this mechanism, the formation of particles with well-defined shapes is impossible. Despite the polydisperse nature of these crystals, the raise in thermodynamic conditions promote a crystal growth process to formation of quasi spherical-shaped β-Ag_2MoO_4 microcrystals were found at 160 °C (see Fig. 9j–l). Recently, (Kumar et al., 2016) reported the formation of this same potato-like β-Ag_2MoO_4 microparticles synthesized by the hydrothermal at 120 °C for 8 h. According to these authors, the CH synthesis promoted to formation of bunches of potatoes-like with clean and fairly smooth surfaces. In our paper, we have observed to same crystal shape to β-Ag_2MoO_4 and at 160 °C the presence of several coral-like β-Ag_2MoO_4 crystals in similarity to the work recently reported by (Oliveira et al., 2017). In addition, these β-Ag2MoO_4 microcrystals exhibits a high level of aggregation and not its possible to measurement of the average size crystal to perform a distribution histogram. However, it is observed that they are in limits ranging from 0.1 to 17 μm. Therefore, these observations clearly indicate that the processing temperature is a key parameter in the morphologic control of β-Ag_2MoO_4 microcrystals.

Fig. 10 shows the illustrate growth process of β-Ag_2MoO_4 microcrystals obtained by te CH method at different temperature for 2 h.

The mechanism to formation and growth process of β-Ag_2MoO_4 microcrystals is shown in the scheme outlined in Fig. 8, in which said process comprises the stages described by Ostwald ripening for growth formation of microcrystals (Vengrenovitch, 1982). Due to the high value of the water dielectric constant (ε = 80 D, 25 °C), the solubility and nucleation of the (Ag_+ and MoO_4^{2-} ions) that make up the starting salts ($AgNO_3$ and $Na_2MoO_4{\cdot}2H_2O$) employed in synthesis precursors at room temperature under constant magnetic stirring. The small particles that underwent nucleation and coalescence in the first stage of the process when subjected to the hydrothermal synthesis at the temperatures assigned in the present study (100, 120 and 140 and 160 °C) underwent multiple rearrangements due to the decrease of the dielectric constant of the water, as well as, due to the increase of the synthesis temperature, thus seeking the equilibrium state of the particles in the interior and surface of the microcrystals, obtaining in the end, coral-like and potatoes-like microcrystals. According to (Gouveia et al., 2014) the formation of β-Ag_2MoO_4 microcrystals using the hydrothermal microwave method using sodium dodecyl sulfate as an anionic surfactant at different temperatures (100–160 °C) for 1 h promotes to growth of cube-like β-Ag_2MoO_4 crystals.

3.6. Photocatalytic activity of β-Ag_2MoO_4 microcrystals for the degradation of RhB dyes

The catalytic assays were performed to degradation of Rhodamine B (RhB) dye molecules using the β-Ag_2MoO_4 microcrystals obtained by hydrothermal synthesis at different temperatures for 1 h are shown in parts of Fig. 11(a)–(e), respectively.

The wavelength of 554 nm was monitored in order to correspond to the absorption maximum for the RhB dye, with a gradual increase in the exposure time to the electromagnetic radiation (UV) in the presence of β-Ag_2MoO_4 microcrystals to reduction of this, implying continuous discoloration of the catalyzed solution. The effect of UV-light in the absence of the catalysts (photolysis) did not show significant degradation/discoloration, thus confirming the stability presented by the RhB molecules in aqueous solution (see Fig. 11a), as well as the relative efficiency of β-Ag_2MoO_4 microcrystals in the catalytic process as shown in Fig. 11(b)–(e). Therefore, we

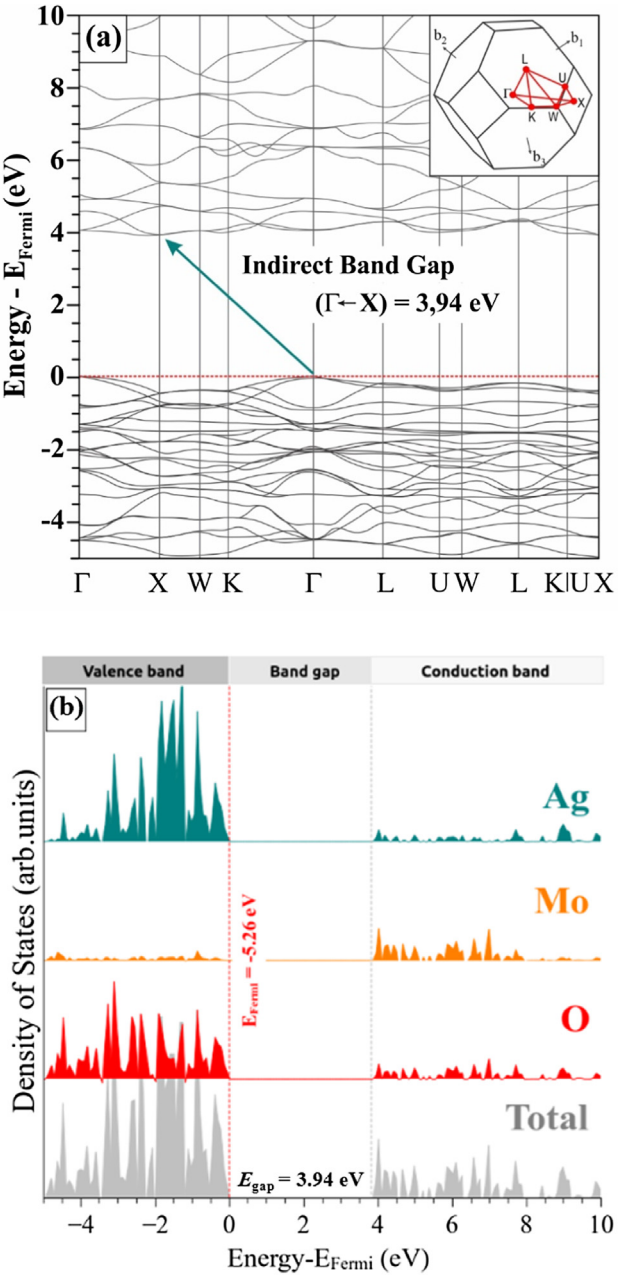

Fig. 7 (a) Electronic band structure showing and indirect band gap, and (b) the projected DOS for β-Ag_2MoO_4 crystal revealing the contribution of each atom to valance and conduction bands. In both panels the top of VB was aligned to Fermi level.

assumed that a high percentage of RhB was destroyed or photodegraded after 120 min under UV light. Moreover, we verified that our β-Ag_2MoO_4 microcrystal catalyst obtained by CH method at 140 °C for 2 h was the most efficient for the degradation of RhB dyes under UV-light.

The plot of the relative concentration of the solution [(C_0-C_n)/C_0] as a function of the exposure time (t/min) respectively. The results of the linearized relative concentration values - ln [($C_0 - C_n$)/C_0] as a function of time (t/min) of exposure to UV-light are shown in Fig. 12(a) and (b).

As it can be noted in Fig. 11(a), we have verified that the β-Ag_2MoO_4 microcrystals synthesized at temperatures of 120 and 140 °C presented the best catalytic performances among all four synthesized and photolysis samples, corresponding to 96.8 and 97.3%, respectively. The apparent velocity constant (k_{app}) for photolysis and solutions catalyzed by β-Ag_2MoO_4 microcrystals obtained by the HC method at different synthesis times for 2 h. The values of k_{app} resulted in the decreasing order $k_{(120\,°C/2h)} > k_{(140\,°C/2h)} > k_{(160\,°C/2h)} > k_{(100\,°C/2h)} > k_{(photolysis)}$, corresponding to k_{app} values equal to: 25.7×10^{-3}, 25.0×10^{-3}, 13.5×10^{-3}, 9.23×10^{-3} and 7.37×10^{-4}, respectively.

The study of the kinetic model of degradation of the RhB dye relative to the catalytic profile of photolysis and microcrystals composed of β-Ag_2MoO_4 microcrystals, obtained by the HC method for 2 h, revealed that the experimental data were better adjusted when the pseudo primer-order model of Langmuir-Hinshelwood (Araújo Júnior et al., 2017) as shown in eq. (13), which best fit the experimental values obtained.

$$t_{1/2} = -\frac{\ln(0.5)}{k_{app}} \tag{13}$$

where k_{app} is correspond to the apparent rate constant of the reaction and $t_{1/2}$ is the half-life time for the dye degradation process. The values obtained are shown for Table 5.

The results presented in this table for β-Ag_2MoO_4 microcrystals synthesized at 120 °C for 2 h is the lowest value of $t_{1/2}$. This being is related to 26.9 min, while for the photolysis to obtain the same percentage of degradation performed by the previously described sample, required 940.5 min, that is, 44.3 times less efficient. Because the β-Ag_2MoO_4 crystal undergoes a photoreduction on its surface by UV light, occurs an improvement in photocatalytic performance by means of formation of by metallic Ag nanoparticles at β-Ag_2MoO_4 surface and can occur from the surface plasmon resonance effect, which these metal Ag nanoparticles due Ag ionic mobility act as electron traps, scattering or absorbing.

The stability of the β-Ag_2MoO_4 was investigated by reusing the microcrystals over three consecutive catalytic cycles initially using 50 mL of 5 mg L^{-1} RhB dye solutions together with 50 mg of the catalyst. In Fig. 13a the result for the three catalytic cycles performed with the microcrystals β-Ag_2MoO_4 synthesized at the temperature of 120 °C are presented. It is clear that the catalysts exhibited catalytic activity over the three consecutive cycles, resulting in the percentages of 97.2, 93.9 and 78.8% degradation of the RhB dye molecules for the first, second and third cycle, respectively. Thus, for the first and second catalytic cycle there were no significant differences in the catalytic performances. Therefore, there was a significant difference when the third cycle was performed. However, the percentage of molecules adsorbed during the 10 min in the absence of UV light is significantly reduced from 15 to 4% when comparing the first and second cycles. These observations can be justified by the mechanism of saturation of the adsorptive capacity of the catalysts in the presence of the RhB dye molecules. The diffraction pattern for the microcrystals β-Ag_2MoO4 collected after the three consecutive catalytic cycles is shown in Fig. 13b. In summary, it was noted that there were no peaks that suggested the formation of secondary phases throughout the photocatalytic process, implying,

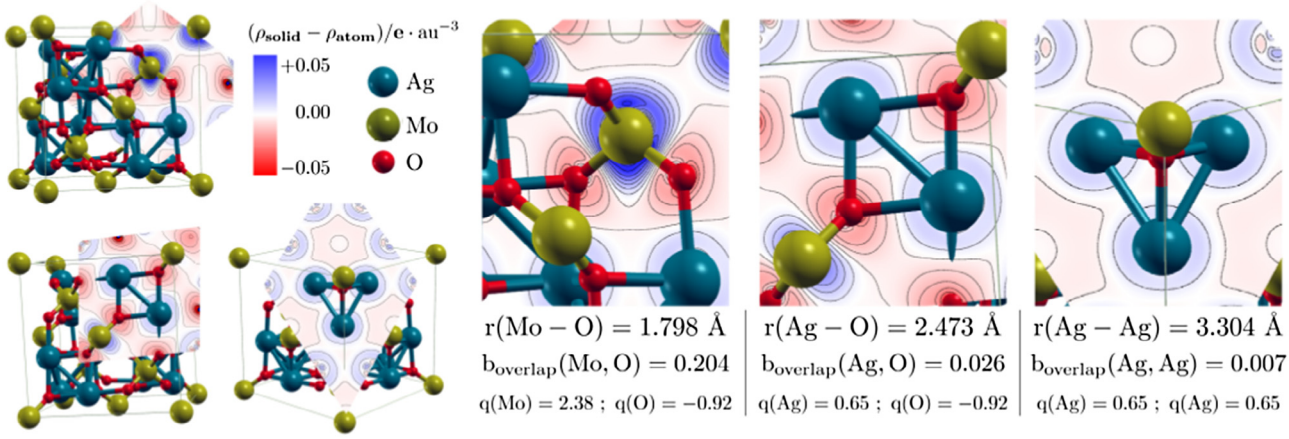

Fig. 8 Charge density difference across three selected bonds: Mo-O, Ag-O and Ag-Ag. Blue and red regions indicates the loss and gain of electrons with respect to isolated atom. The Mulliken population analyses shows a higher overlap inside tetrahedral [MoO_4] clusters when compared with octahedral [AgO_6] clusters, and negligible for Ag ↔ Ag iteration. The Mulliken charges follow the same trend of expected classical oxidation state for all atoms.

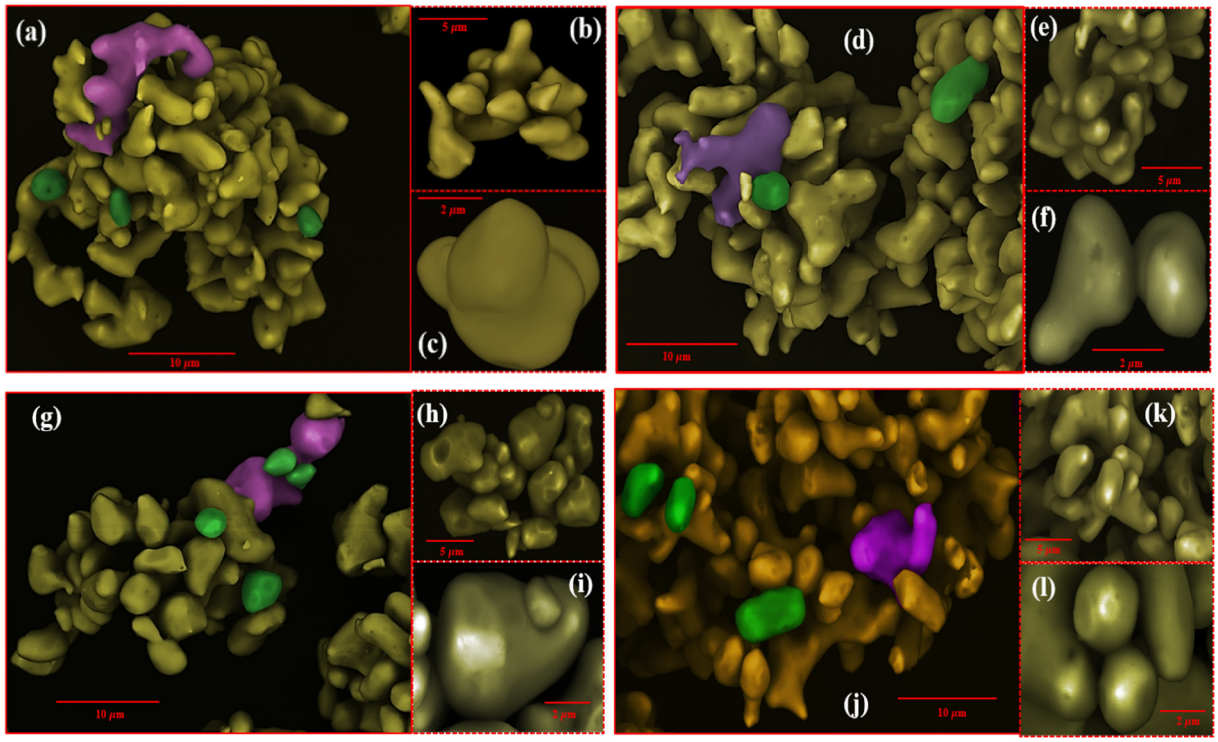

Fig. 9 FE-SEM images and EDS for β-Ag_2MoO_4 microcrystals obtained from HC method in the temperatures: 100 °C (a, b and c); 120 °C (d, e and f); 140 °C (g, h and i); 160 °C (j, k and l) for 2 h.

therefore, the high stability of the microcrystals against the photocatalytic tests.

3.7. A possible photocatalytic mechanism for the degradation of RhB dyes by β-Ag_2MoO_4 microcrystals

Fig. 14 shows the proposed scheme for the excitation/recombination processes occurring in the band structures (BV and BC) of silver molybdenum microcrystals when irradiated with wavelength radiation in the UV region (252 nm) in aqueous medium.

In these processes it is of fundamental importance to consider the mechanism of adsorption of the species present in the reaction medium, so that the period of 10 min under ultrasonic agitation in the absence of light is necessary to reach the equilibrium of adsorption of the dye with the microcrystals, as well as the water and oxygen molecules available in the system (Cavalcante et al., 2012a,b,c,d). The heterogeneous photocatalysis basically consists of the catalysis initiated by the

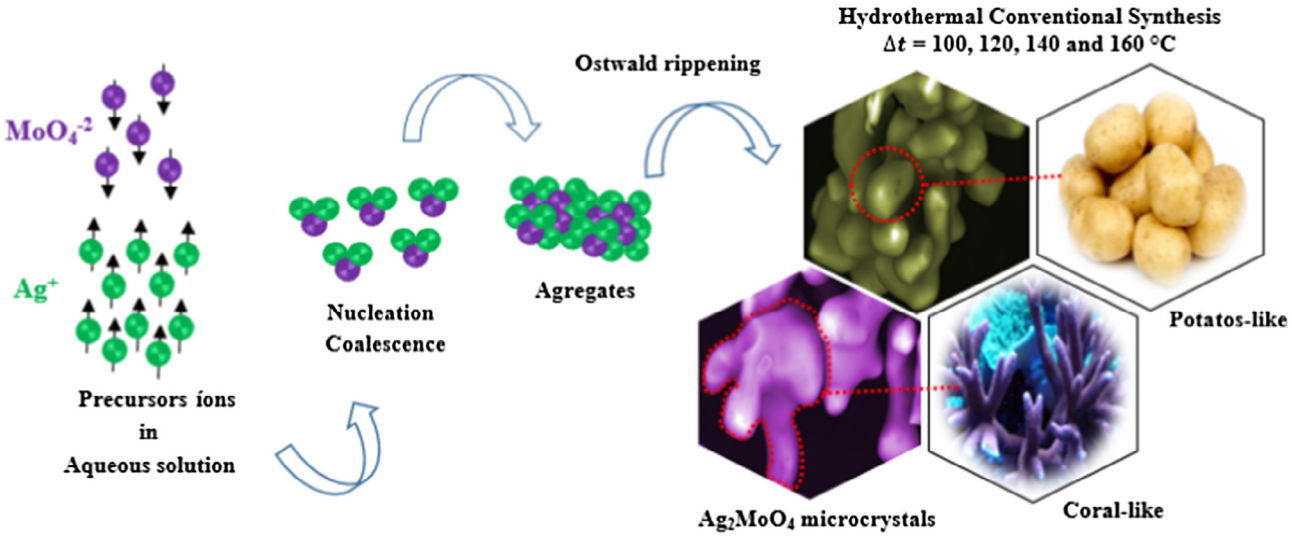

Fig. 10 Scheme of formation and growth process for β-Ag_2MoO_4 microcrystals synthesized by the CH method at different synthesis temperatures (100, 120, 140 and 160 °C) for 2 h, resulting in coral-like and potatos-like β-Ag_2MoO_4 microcrystals.

oxidative processes results of the energy photon absorption mechanism with magnitude equal to or greater than the value of Egap (hν ≥ Egap) that limits the BV, where it is filled with electrons for the BC, electron-deficient region, with intermediate levels in this range (Feltrin et al., 2013). Electron excitation of the electrons (′) from BV to BC results in the formation of holes (●) in the structures, which act as oxidants to adsorbed water molecules on the surface of β-Ag_2MoO_4 microcrystals, resulting in the formation of H^+ ions and hydroxyl radicals ($OH^{\bullet}$) (Roca et al., 2005) as shown in Fig. 13.

The unit cell for β-Ag_2MoO_4 microcrystals is composed of distorted octahedral [AgO_6] clusters and tetrahedral [MoO_4] clusters, which depending on numerous factors may exhibit greater or lesser amounts of crystalline defects, of vacancy oxygen (V_0^x), distortions in lattice related to phenomenon to order-disorder at medium range, generating species of complex clusters presentes into VB and complex clusters located main in BC (Cavalcante et al., 2012a,b,c,d). In addition, other factors may be considered essential in the catalytic process, highlighting the surface energy (Roca et al., 2015) presence of impurities (Vogt, Weckhuysen, and Ruiz-Martínez, 2017), particle size and shape and preferential orientation (Cheng, Li, and Schlaberg, 2016; Liu et al., 2010).

The process of excitation/recombination of electrons in the internal structures of β-Ag_2MoO_4 microcrystals is initiated by the absorption of the photon ($h\nu$) with energy of magnitude equal or superior to 4.92 eV (UV-light) ($E_{gap} \geq 3.35$ eV), in the absence of this process, it is important to note that along the surface and internal structures of the microcrystals the defects and distortions caused by them imply polarization resulting in the ordered electronic transitions clutter in the clusters (Cavalcante et al., 2012a,b,c,d). The polarization processes occurring in the clusters present in the microstructures of silver molybdenites are shown in Eqs. (14) and (15) below:

$$\beta - Ag_2MoO_{4(defects)} \rightarrow [MoO_4]_d^x - [MoO_4]_o^x \quad (14)$$

$$\beta - Ag_2MoO_{4(defects)} \rightarrow [AgO_6]_d^x - [AgO_6]_o^x \quad (15)$$

After the absorption of electromagnetic radiation by the microcrystals, there is formation of the electron/holes pairs in the complex clusters present in the unit cell, resulting, therefore, in the pairs $[MoO_4]_d - [MoO_4]_o e [AgO_6]_d - [AgO_6]_o$. In aqueous media, they adsorb the water molecules present on the surface of the microcrystals, which in the face of the formed holes, oxidize the water molecules to radicals (HO) and hydrons (H^+) as shown in Eqs. (16)–(21):

$$\beta - Ag_2MoO_{4(defects)} \rightarrow h\nu = 4.92eV [MoO_4]_d^x - [MoO_4]_o^x \rightarrow [MoO_4]_d - [MoO_4]_o \quad (16)$$

$$\beta - Ag_2MoO_{4(defects)} \rightarrow h\nu = 4.92eV [A_gO_6]_d^x - [A_gO_6]_o^x \rightarrow [A_gO_6]_d - [A_gO_6]_o \quad (17)$$

$$[MoO_4]_d + H_2O \rightarrow [MoO_4]_d ... H_2O_{(ads)} \quad (18)$$

$$[MoO_4]_d ... H_2O_{(ads)} \rightarrow [MoO_4]_d^x + HO + H^+ \quad (19)$$

$$[A_gO_6]_d + H_2O \rightarrow [A_gO_6]_d ... H_2O_{(ads)} \quad (20)$$

$$[A_gO_6]_d ... H_2O_{(ads)} \rightarrow [A_gO_6]_d^x + HO + H^+ \quad (21)$$

The electrons excited to the CB are captured by numerous species that are present in the reaction medium, thus avoiding the return of these to the VB (Schneider et al., 2014). Oxygen (O_2) is usually diluted in aqueous systems, which is considered to be one of the main electron capture species for the formation of the superoxide radical anion (O_2), which once in the presence of hydronium (H^+) react resulting in the radical hydroperoxide (O_2H), represented by Eqs (22)–(25):

$$[MoO_4]_d + O_2 \rightarrow [MoO_4]_d ... O_2 \quad (22)$$

$$[MoO_4]_d ... O_2 + H^+ \rightarrow [MoO_4]_d^x ... O_2H \quad (23)$$

$$[AgO_6]_d + O_2 \rightarrow [AgO_6]_d ... O_2 \quad (24)$$

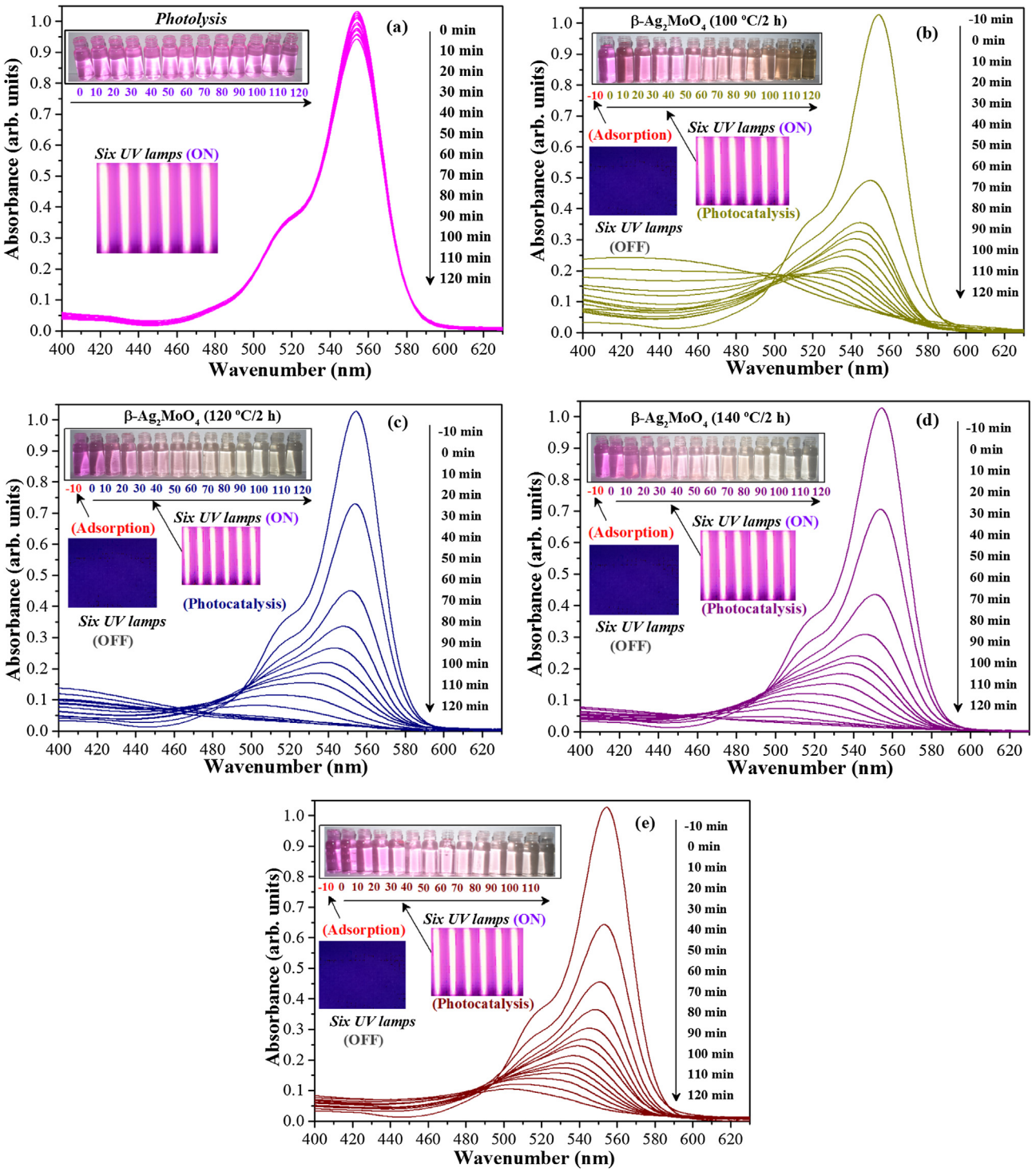

Fig. 11 Evolution of UV–vis absorption spectra from after 120 min of illumination for photodegradation of RhB dye solution: (a) photolysis and by the catalysts β-Ag_2MoO_4 microcrystals synthesized at the temperature of 100 (b), 120 (c), 140 (d) and (e) 160 °C, respectively.

$$[AgO_6]_d...O_2 + H^{+\rightarrow}[AgO_6]_d^x...O_2H \quad (25)$$

The RhB dye molecules themselves absorb electromagnetic radiation, called photolysis, resulting in the breaking of the carbon chains generating by-products by the process described as mineralization (Tian et al., 2016). However, the oxidative processes generated by the $O_2H^{\cdot}$ and HOradicals using β-Ag_2MoO_4 microcrystals as catalyst are of higher evaluation, considering that in the present study the photolysis composed only 8.7% of the percentage of degradation during 2 h of catalysis, whereas for the microcrystals, there was for the sample synthesized at 140 °C, 97.3% degradation of RhB dye molecules for 2 h of exposure to UV-light, resulting in higher rate

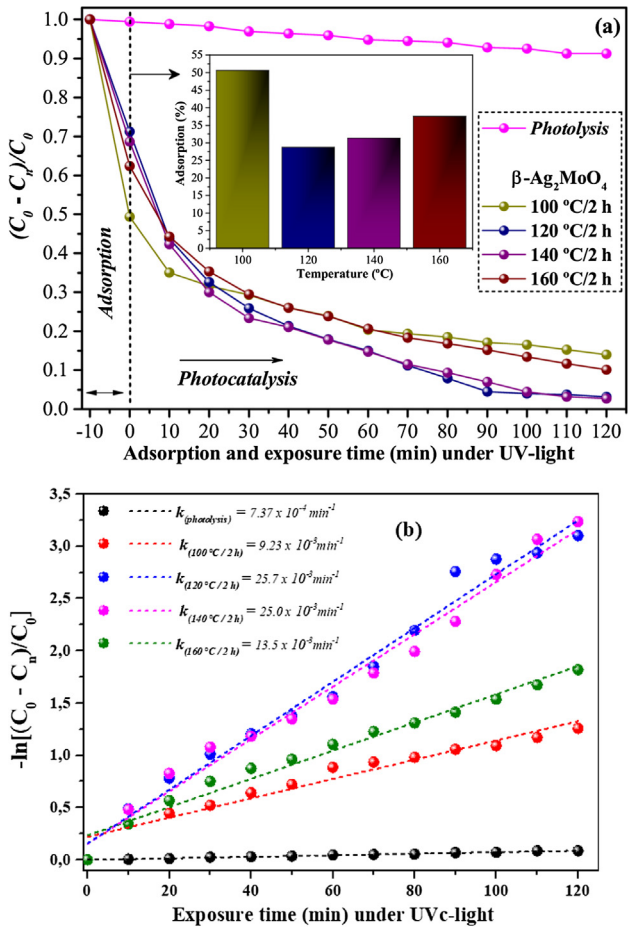

Fig. 12 (a) Evolution of the catalysis of the RhB dye as a function of time (min) of exposure to UV-light and (b) First-order kinetics: without catalysts and with catalysts β-Ag_2MoO_4 microcrystals synthesized at the temperatures (100, 120, 140 and 160 °C0 for 2 h, respectively.

of radical formation O_2H and HO radicals e por consequência, descoloração and degradation of the RhB dye molecules presentes in aqueloes solutions (Barreiros, David and David, 2006), can be observed in Eqs. (26) and (27) below:

$$\rightarrow h\nu = 4.92eV\text{RhB} \rightarrow RhB \tag{26}$$

$$RhB \rightarrow O_2H \vee HO\text{CCO} + \text{H}_2\text{O} + \text{CO}_2 \tag{27}$$

where CCO = colorless compounds organic.

Based on this photocatalytic mechanism, we assume that the defects on the crystal surface and the electronic structure of the complex distorted/disordered $[AgO_6]_d$ and $[MoO_4]_d$ complex clusters and ordered $[AgO_6]_o$ and $[MoO_4]_o$ complex clusters display an important role in the production of O_2H and HO radicals, which are the most oxidizing species in these chemical reactions for the degradation of the organic RhB dye in aqueous solution.

4. Conclusions

In summary, microcrystals of β-Ag_2MoO_4 were obtained by the hydrothermal method at different temperatures (100–160 °C) for 2 h. The structural (XRD and Rietveld) and vibrational characterizations according to experimental and theoretical active modes of symmetry (Raman and FTIR) revealed the formation of microcrystals in beta phase (β-Ag_2MoO_4) with cubic structure and space group Fd3′m without the presence of secondary phase. The values of E_{gap} obtained by Uv–vis by diffuse reflectance resulted in a direct relation of the decrease of E_{gap} with the addition of the temperature assigned in the hydrothermal synthesis, being these in good agreement with the information obtained by the computational study by DFT using DOS, the contributions of the silver orbitals – Ag ($4d_{xy}$ + $4d_{xz}$ + $4d_{yz}$ + $4d_{x^2-y^2}$ + $4d_{z^2}$) and oxygen – O ($2p_x$ + $2p_y$ + $2p_z$) in the valence band and the molybdenum atoms – Mo ($4d_{xy}$ + $4d_{xz}$ + $4d_{yz}$ + $4d_{x^2-y^2}$ + $4d_{z^2}$) and oxygen – O ($2p_x$ + $2p_y$ + $2p_z$) in the conduction band. The FE-SEM images of Ag_2MoO_4 microcrystals presented a coral-like and potatoes-like format for all the synthesis temperatures attributed to the hydrothermal synthesis, a result of the nucleation process, coalescence and microcrystals growth by the Ostwald ripening mechanism, obtaining microcrystals ranging in size from 94.285 to 99.808 nm. The catalytic assays of the microcrystals of β-Ag_2MoO_4 in the photodegradation of the Rhodamine B dye (RhB) in the interval of 2 h under UVc radiation, resulted in the best catalytic performances for the microcrystals synthesized in the temperatures of 120 and 140 °C, obtaining values of constant of the apparent velocity and the half-life time of 25.0×10^{-3} min^{-1}, 27.7 min and 25.7×10^{-3} min^{-1}, 26.9 min, respectively, with crystallite defects participation, clusters deformations [AgO_6] and [MoO_4], as well as vacancies of the oxygen atoms along the crystal lattice. The stability of the β-Ag_2MoO_4 was investigated by reusing the microcrystals over three consecutive catalytic cycles, resulting in the percentages of 97.2, 93.9 and 78.8% degradation of the RhB dye molecules for the first,

Table 5 Experimental results of size crystal ($\bar{D}_{hkl}$), degradation rate, kinetic constant (k_{app}) and half-life time ($t_{1/2}$) values of β-Ag_2MoO_4 microcrystals.

ID	$\bar{D}_{hkl}$ (nm)	Degradation (%)	$k_{app} \times 10^{-3}$ (min^{-1})	$t_{1/2}$ (min)
Photolysis	–	8.7	0.73	940.5
100 °C/2h	99.606(4)	85.8	9.23	75.0
120 °C/2h	96.808(4)	97.3	25.7	26.9
140 °C/2h	99.123(4)	96.8	25.0	27.7
160 °C/2h	94.285(2)	89.9	13.5	51.3

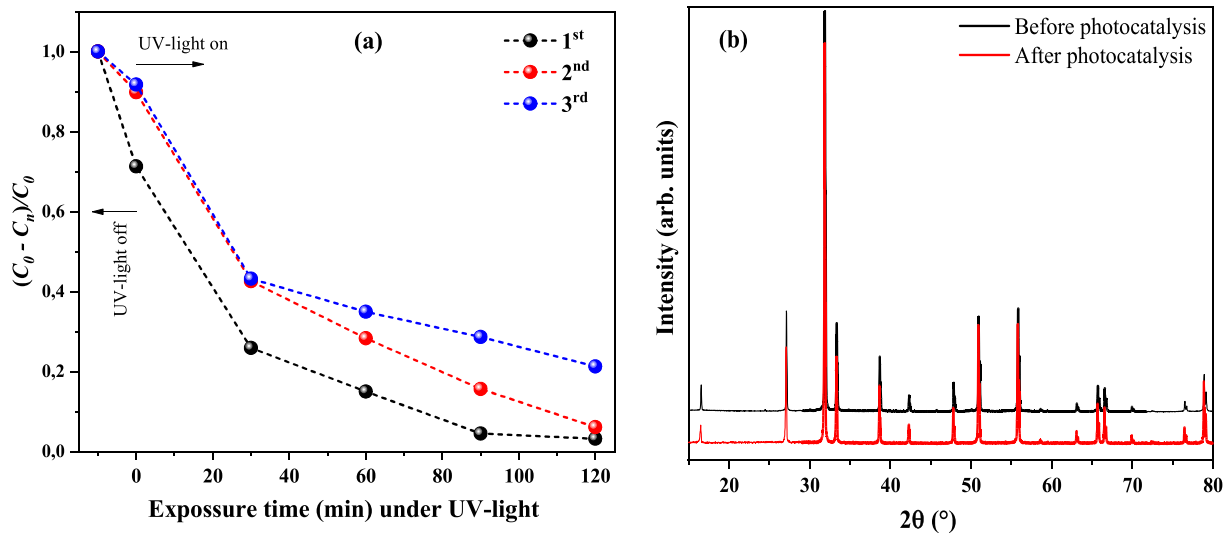

Fig. 13 (a) Reusability and (b) diffraction pattern for β-Ag_2MoO_4 microcrystals the in three consecutive cycles.

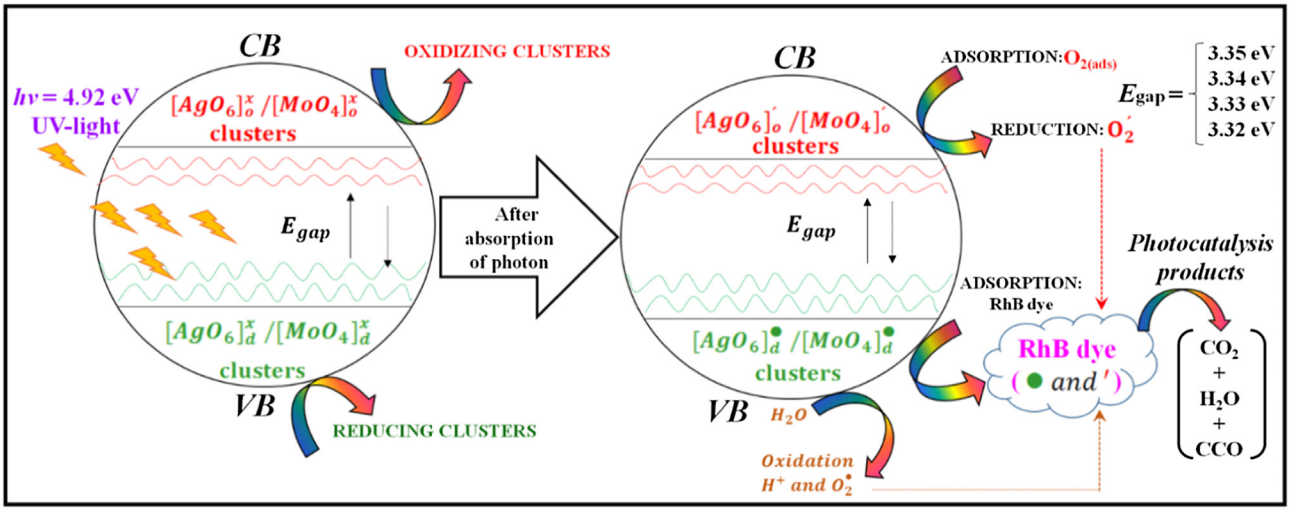

Fig. 14 Scheme of electron excitation/recombination process during, illumination with UV-light of β-Ag_2MoO_4 microcrystals in solutions of RhB dyes, band structures and mineralization of Rhodamine B (RhB) dye molecules.

second and third cycle, respectively. The diffraction pattern for the microcrystals β-Ag_2MoO_4 collected after the three consecutive catalytic cycles suggested that the no formation of secondary phases throughout the photocatalytic process, imply the high stability of the microcrystals against the photocatalytic tests.

5. Notes

The authors declare no conflict of interest.

Acknowledgements

The authors acknowledge the financial support of the Brazilian research financing institutions: National Council for Scientific and Technological Development (CNPq) (304261/2009-2, 479644/2012-8 and 304531/2013-8), Research Support Foundation of Piauí State (FAPEPI), and Foundation for the Coordination and Improvement of Higher Level or Education Personnel(CAPES).

References

Andrés, J., Ferrer, M.M., Gracia, L., Beltran, A., Longo, V.M., Cruvinel, G.H., Tranquilin, R.L., Longo, E., 2015. A Combined experimental and theoretical study on the formation of ag filaments on β-Ag_2MoO_4 induced by electron irradiation. Part. Part. Syst. Char. 32 (6), 646–651.

Araújo Júnior, E.A., Nobre, F.X., Sousa, G.S., Cavalcante, L.S., Santos, M.R.M.C., Souza, F.L., Matos, J.M.E., 2017. Synthesis, growth mechanism, optical properties and catalytic activity of ZnO microcrystals obtained via hydrothermal processing. RSC Adv. 7, 24263–24281.

Arora, A.K., Nithya, R., Misra, S., Yagi, T., 2012. Behavior of silver molybdate at high-pressure. J. Solid State Chem. 196, 391–397.

Barreiros, A.L.B.S., David, J.M., David, J.P., 2006. Estresse oxidativo: Relação entre geração de espécies reativas e defesa do organismo. Quim. Nova 29, 113–123.

Becke, A.D., 1993. Density-functional thermochemistry. III. The role of exact exchange. J. Chem. Phys. 98, 5648–5652.

Beltrán, A., Gracia, L., Longo, E., Andrés, J., 2014. First-principles study of pressure-induced phase transitions and electronic properties of Ag_2MoO_4. J. Phys. Chem. C 118, 3724–3732.

Canepa, P., Hanson, R.M., Ugliengo, P., Alfredsson, M., 2011. J-ICE: a new Jmol interface for handling and visualizing crystallographic and electronic properties. J. Appl. Crystallogr. 44, 225–229.

Cao, W., An, Y., Chen, L., Qi, Z., 2017. Visible-light-driven Ag_2MoO_4/Ag_3PO_4 composites with enhanced photocatalytic activity. J. Alloys Compd. 701, 350–357.

Cavalcante, L.S., Longo, V.M., Sczancoski, J.C., Almeida, M.A.P., Batista, A.A., Varela, J.A., Orlandi, M.O., Longo, E., Siu, M.S., 2012a. Electronic structure, growth mechanism and photoluminescence of $CaWO_4$ crystals. CrystEngComm 14, 853–868.

Cavalcante, L.S., Almeida, M.A.P., Avansi, W.J., Tranquilin, R.L., Longo, E., Batista, N.C., Mastelaro, V.R., Li, M.S., 2012b. Cluster coordination and photoluminescence properties of α-Ag_2WO_4 microcrystals. Inorg. Chem. 51, 10675–10687.

Cavalcante, L.S., Batista, F.M.C., Almeida, M.A.P., Rabelo, A.C., Nogueira, I.C., Batista, N.C., Varela, J.A., Santos, M.R.M.C., Longo, E., Li, M.S., 2012c. Structural refinement, growth process, photoluminescence and photocatalytic properties of $(Ba_{1-x}Pr_{2x/3})WO_4$ crystals synthesized by the coprecipitation method. RSC Adv. 2, 6438–6454.

Cavalcante, L.S., Sczancoski, J.C., Li, M.S., Longo, E., Varela, J.A., 2012d. β-$ZnMoO_4$ microcrystals synthesized by the surfactant-assisted hydrothermal method: Growth process and photoluminescence properties. Coll. Surf. A. Physicochem. Eng. Aspects. 396, 346–351.

Cavalcante, L.S., Moraes, E., Almeida, M.A.P., Dalmaschio, C.J., Batista, N.C., Varela, J.A., Longo, E., Li, M.S., Andrés, J., Beltrán, A., 2013. A combined theoretical and experimental study of electronic structure and optical properties of β-$ZnMoO_4$ microcrystals. Polyhedron 54, 13–25.

Cheng, W., Li, Y., Schlaberg, H.I., 2016. The size effect of titanium dioxide particles on desulfurization in a power plant. Bulgarian Chem. Commun. 48, 219–225.

Cunha, F.S., Sczancoski, J.C., Nogueira, I.C., de Oliveira, V.G., Lustosa, S.M.C., Longo, E., Cavalcante, L.S., 2015. Structural, morphological and optical investigation of β-Ag_2MoO_4 microcrystals obtained with different polar solvents. CrystEngComm 17, 8207–8211.

Dovesi, R., Saunders, V.R., Roetti, C., Orlando, R., Zicovich-Wilson, C.M., Pascale, F., Civalleri, B., Doll, K., Harrison, N.M., Bush, I. J., D'Arco, P., Llunell, M., Causà, M., Noël, Y., Maschio, L., Erba, A., Rerat, M., Casassa, S., 2017. CRYSTAL17 User's Manual. University of Torino, Torino.

Erba, A., Baima, J., Bush, I., Orlando, R., Dovesi, R., 2017. Large-scale condensed matter DFT simulations: performance and capabilities of the CRYSTAL code. J. Chem. Theory Comput. 13 (10), 5019–5027.

Fabbro, M.T., Foggi, C.C., Santos, L.P.S., Gracia, L., Perrin, A., Perrin, C., Vergani, C.E., Machado, A.L., Andrés, J., Cordoncill, E., Longo, E., 2016. Synthesis, antifungal evaluation and optical properties of silver molybdate microcrystals in different solvents: a combined experimental and theoretical study. Dalton Trans. 45, 10736–10743.

Feltrin, J., Sartor, M.N., Bernardin, A.M., Hotza, D., Labrincha, J.A., Santa, U.F., Aveiro, U., 2013. Parte I: Síntese, estrutura e fotoatividade, 59, 620–632.

Feng, M., Zhang, M., Song, M., Li, X.-G., Yu, S.-H., 2011. Ultralong silver trimolybdate nanowires: Synthesis, phase transformation, stability, and their photocatalytic, optical, and electrical properties. ACS Nano 5, 6726–6735.

Gouveia, A.F., Sczancoski, J.C., Ferrer, M.M., Lima, A.S., Santos, M. R.M.C., Li, M.S., Longo, E., Cavalcante, L.S., 2014. Experimental and theoretical investigations of electronic structure and photoluminescence properties of β-Ag_2MoO_4 microcrystals. Inorg. Chem. 53, 5589–5599.

Grimme, S., Antony, J., Ehrlich, S., Krieg, H., 2010. J. Chem. Phys. 132, 154104.

Gupta, S.K., Ghosh, P.S., Sudarshan, K., Gupta, R., Pujari, P.K., Kadam, R.M., 2015. Multifunctional pure and Eu^{3+} doped β-Ag_2MoO_4: photoluminescence, energy transfer dynamics and defect induced properties. Dalton Trans. 44, 19097–19110.

Kassou, S., El Mrabet, R., Kaiba, A., Guionneau, P., Belaaraj, A., 2016. Combined experimental and density functionaltheory studies of an organic–inorganichybrid perovskite. PCCP 18, 9431–9436.

Kokalj, A., 2003. Computer graphics and graphical user interfaces as tools in simulations of matter at the atomic scale. Compt. Mater. Sci. 28, 155–168.

Kroumova, E., Aroyo, M.I., Perez-Mato, J.M., Kirov, A., Capillas, C., Ivantchev, S., Wondratschek, H., 2003. Bilbao Crystallographic Server: Useful databases and tools for phase-transition studies. Phase Trans. 76, 155–170.

Kubelka, P., Munk, F., 1931. Ein Beitrag Zur Optik Der Farbanstriche. Zeit. Für. Tech. Physik. 12, 593–601.

Kumar, J.V., Karthik, R., Chen, S.-M., Muthuraj, V., Karuppiah, C., 2016. Fabrication of potato-like silver molybdate microstructures for photocatalytic degradation of chronic toxicity ciprofloxacin and highly selective electrochemical detection of H_2O_2. Sci. Rep. 6, 34149–34162.

Lee, C., Yang, W., Parr, R.G., 1988. Development of the Colle-Salvetti correlation-energy formula into a functional of the electron density. Phys. Rev. B 37 (2), 785–789.

Liu, M., Piao, L., Zhao, L., Ju, S., Yan, Z., He, T., Zhou, C., Wang, W., 2010. Anatase TiO2 single crystals with exposed 001 and 110 facets: facile synthesis and enhanced photocatalysis. Chem. Commun. 46, 1664–1666.

Longo, E., Volanti, D.P., Longo, V.M., Gracia, L., Nogueira, I.C., Almeida, M.A.P., Pinheiro, A.N., Ferrer, M.M., Cavalcante, L.S., Andrés, J., 2014. toward an understanding of the growth of Ag filaments on α-Ag_2WO_4 and their photoluminescent properties: a combined experimental and theoretical study. J. Phys. Chem. C 118, 1229–1239.

Ferrero, M., Rerat, M., Kirtman, B., Dovesi, R., 2008a. Calculation of first and second static hyperpolarizabilities of one- to three-dimensional periodic compounds. Implementation in the CRYSTAL code. J. Chem. Phys. 129, 244110 (1–13).

Ferrero, M., Rerat, M., Kirtman, B., Dovesi, R., 2008b. The calculation of static polarizabilities of 1–3D periodic compounds. the implementation in the crystal code. J. Comput. Chem. 29, 1450–1459.

Mith, A.M., Nie, S., 2010. Semiconductor nanocrystals: Structure, properties, and band gap engineering. Acc. Chem. Res. 43 (2), 190–200.

Momma, K., Izumi, F., 2011. VESTA 3 for three-dimensional visualization of crystal, volumetric and morphology data. J. Appl. Crystallogr. 44, 1272–1276.

Morales, A.E., Mora, E.S., Pal, U., 2007. Use of diffuse reflectance spectroscopy for optical characterization of un-supported nanostructures. Rev. Mex. Fis. S. 53, 18–22.

Moura, J.V.B., da Silva Filho, J.G., Freire, P.T.C., Luz-Lima, C., Pinheiro, G.S., Viana, B.C., Filho, J.M., Souza-Filho, A. G., Saraiva, G.D., 2016. Phonon properties of β-Ag_2MoO_4: Raman spectroscopy and ab initio calculations. Vib. Spectrosc. 86, 97–102.

Moura, J.V.B., Freitas, T.S., Cruz, R.P., Pereira, R.L.S., Silva, A.R.P., Santos, A.T.L., da Silva, J.H., Luz-Lima, C., Freire, P.T.C., Coutinho, H.D.M., 2017. β-Ag_2MoO_4 microcrystals: characterization, antibacterial properties and modulation analysis of antibiotic activity. Biomed. Pharmacot. 86, 242–247.

Ng, C.H.B., Fan, W.Y., 2015. Uncovering Metastable α-Ag_2MoO_4 phase under ambient conditions. overcoming high pressures by 2,3-bis(2-pyridyl)pyrazine doping. Cryst. Growth Des. 15, 3032–3037.

Ng, C.H.B., Fan, W.Y., 2017. Crystal origami: preparation of β-Ag_2MoO_4 concave and convex crystals with high-index facets. ChemNanoMat 3, 178–182.

Oliveira, C.A., Volanti, D.P., Nogueira, A.E., Zamperini, C.A., Vergani, C.E., Longo, E., 2017. Well-designed β-Ag_2MoO_4 crystals with photocatalytic and antibacterial activity. Mater. Des. 115, 73–81.

Piasecki, M., Mandowska, E., Herrmann, A., Ehrt, D., Majchrowski, A., Jaroszewicz, L.R., Brik, M.G., Kityk, I.V., 2015. Tailoring Nd3 + luminescence characteristics by Yb3+ doping in K5Nd(MoO4) 4, RbNd(WO4)2 and NdAl3(BO3)4 crystal matrices. J. Alloys Compd. 639, 577–582.

Lacomba-Perales, R., Ruiz-Fuertes, J., Errandonea, D., Martínez-García, D., Segura, A., 2008. Optical absorption of divalent metal tungstates: correlation between the band-gap energy and the cation ionic radius. Eur. Phys. Lett. 83, 37002–37006.

Rodriguez-Carvajal, J., 2010. Full Comput. Program. http://www.ill.eu/sites/fullprof/php/downloads.html.

Schneider, J., Matsuoka, M., Takeuchi, M., Zhang, J., Horiuchi, Y., Anpo, M., Bahnemann, D.W., 2014. Understanding TiO_2 photocatalysis : mechanisms and materials. Chem. Rev. 114, 9919–9986.

Smith, R.A., 1978. Semiconductors. Cambridge University Press, London, p. 434.

Som, S., Sharma, S.K., 2012. Eu^{3+}/Tb^{3+}-codoped Y_2O_3 nanophosphors: rietveld refinement, bandgap and photoluminescence optimization. J. Phys. D.: Appl. Phys. 45, 415102–415112.

Tang, H., Fu, Y., Chang, S., Xie, S., Tang, G., 2017. Construction of Ag_3PO_4/Ag_2MoO_4 Z-scheme heterogeneous photocatalyst for the remediation of organic pollutants. Chin. J. Catal. 38, 337–347.

Tian, J., Zhao, J., Olajuyin, A.M., Sharshar, M.M., Mu, T., Yang, M., Xing, J., 2016. Effective degradation of Rhodamine B by electro-Fenton process, using ferromagnetic nanoparticles loaded on modified graphite felt electrode as reusable catalyst: in neutral pH condition and without external aeration. Environm. Sci. Poll. Res. 23, 15471–15482.

Vengrenovitch, R.D., 1982. On the Ostwald ripening theory. Acta Metall. 30 (6), 1079–1086.

Vogt, C., Weckhuysen, B.M., Ruiz-Martínez, J., 2017. Effect of feedstock and catalyst impurities on the methanol-to-olefin reaction over H-SAPO-34. ChemCatChem 9, 183–194.

Wang, Z., Daí, K., Liang, C., Zhang, J., Zhu, G., 2017. Facile synthesis of novel butterfly-like Ag_2MoO_4 nanosheets for visible-light driven photocatalysis. Mater. Lett. 196, 373–376.

Wyckoff, R.W.G., 1922. The crystal structure of silver molybdate. J. Am. Chem. Soc. 44, 1994–1998.

Zhang, J., Ma, Z., 2017a. Flower-like Ag_2MoO_4/Bi_2MoO_6 heterojunctions with enhanced photocatalytic activity under visible light irradiation. J. Taiwan Inst. Chem. Eng. 71, 156–164.

Zhang, J., Ma, Z., 2017b. Novel β-Ag_2MoO_4/g-C_3N_4 heterojunction catalysts with highly enhanced visible-light-driven photocatalytic activity. RSC Adv. 7, 2163–2171.

Rietveld, H.M., 1967. Line profiles of neutron powder-diffraction peaks for structure refinement. Acta Crystallograp. 22, 151–152.

Zhou, D., Li, Jing, Pan, L.-X., Wang, D.-W., Reaney, I.M., 2017. Novel water insoluble $(Na_xAg_{2x})MoO_4$ ($0 \leq x \leq 2$) microwave dielectric ceramics with spinel structure sintered at 410 degrees. J. Mater. Chem. C 5, 6086–6091.